Feasibility study of components manufactured using additive technology for the electrical sector

Michele Quercio

* * * * *

Supervisors
Prof. A. Canova, Supervisor
Prof. C. Ragusa, Co-supervisor

Doctoral Examination Committee:
Prof. A. Cristofolini, Referee, Università Di Bologna
Prof. A. Laudani, Referee, Università degli Studi Roma Tre
Prof. F. Freschi, Politecnico di Torino
Prof. L. Giaccone, Politecnico di Torino
Dr. D. Giordano, Istituto Nazionale di Ricerca Metrologica

I hereby declare that, the contents and organisation of this dissertation constitute my own original work and does not compromise in any way the rights of third parties, including those relating to the security of personal data.

....

Michele Quercio

Turin, 2022

Summary

This research work addresses the application of Additive Manufacturing (AM) technologies for the production of ferromagnetic components. The design freedom offered by AM allow to realize component with complex geometry, so new geometries can be made for the most common applications such as the electric motors. The thesis explore the possibility offered by AM to improve ferromagnetic objects for lightweight and high performance point of view, with potential in several industrial sectors. First of all, the printing technique that best lends itself to the production of these components was investigated. From the studies carried out, it appears that the optimal technique is the Laser Powder Bed Fusion (LPBF). After the technique was identified, the printing parameters that influence the microstructural properties and consequently the mechanical, electrical and magnetic properties were characterized. Subsequently, post-processing heat-treatments were analyzed to undestand its influence on the magnetic properties. The results of this research show that, by means of LPBF, silicon steel parts with permeability ($\simeq$ 3000) and hysteresis loss ($\simeq$ 85.6 A/m) can be produced. Two new applications, compared to the technical literature, are presented. A plug of an electromagnet and an electromagnetic shield. The results of the first application made it possible to understand some limitations of the printing technology. For example, the creation of small axial-symmetric objects involves a tolerance with respect to the axis of revolution to be taken into consideration. The application of the electromagnetic screen is completely innovative as there are no applications of this kind in scientific literature. The results show good shielding properties for this kind of material, especially after annealing.Finally, we propose that further research should be aimed at expanding the range of applicability of this printed material , as well as at the adapting of the alloy's chemistry for improved ductility to avoid the risk of in-process cracking.

Acknowledgements

I would like to dedicate this thesis to my loving parents and my grandparents

Contents

List of Tables

List of Figures

Chapter 1

Introduction

Additive manufacturing (AM) can positively affect energy savings from the point of view of consumption. The improvement of the efficiency of motors in the field of transport, for example, depends on the ability to reduce losses (thermal, mechanical, drive) during their normal operation. Improving engine efficiency affects fuel consumption (for vehicles fossil fuel powered) or electricity (for electric vehicles). Additive manufacturing can be used to modify existing production methods and the materials used in current technologies for the development of energy in general or the production of electricity. For example, the production of turbines, heat exchangers or specific parts of current systems through this innovative technology to replace traditional ones. With specific reference to the production process of new metal components for improvement of efficiency related to both energy production and consumption, additive techniques, compared to traditional subtractive offer the following potential advantages:

- Reduction of the time of realization;

- Total absence of limits to the geometry of the products to be made;

- Possibility of geometric optimization and consequent drastic reduction of the quantity of material used;

- Exploitation of the material to its maximum capacity;

- Possibility of creating complex pieces in single and unassembled blocks;

- Normally, reduction of energy consumption;

- Possibility of using innovative and more efficient materials;

By comparing costs, it is easy to understand how as the complexity of the object increases, the costs of the additive manufacturing tends to match those of traditional manufacturing until, beyond a certain degree of complexity of the prototype to be made, additive manufacturing allows for costs considerably reduced, not requiring lengthy mechanical processing, assembly, and welding of the components and, in the case of castings, the creation of molds. [1],[2]. The family of additive manufacturing processes is particularly attractive for the production efficiency of items that would otherwise have a high buy-to-fly ratio [3]. The buy-to-fly ratio is simply the ratio of the mass between the starting material and the final one, that of the finished part. Buy-to-fly ratios of 10 to 1 (i.e., only 10% of the original material remains in the finished product) are common in aerospace applications for parts produced through traditional subtractive manufacturing processes [3]. High buy-to-fly ratios are achieved, especially when the geometry of the finished part requires a larger starting block, and most of the volume is removed and thrown away. This weight reduction is critical not only for the aerospace and automotive market but also in the medical, and biotechnology sectors, as it allows a significant reduction in energy and ease of use [4]. Intuitively, it seems clear that the production of parts through subtractive manufacturing requires removing most of the starting material and requires a more significant amount of energy compared to additive manufacturing. On the contrary, in cases where little material is removed, the manufacture subtractive may require less energy overall [5]. In subtractive manufacturing, all the processes that lead to the final product must be included. Examples are drilling, turning, milling, carving, grinding. During the additive manufacturing process, energy is required for the transport of the stored material, obtain and maintain the appropriate thermal and atmospheric conditions, and activate the motors for the phases of positioning of objects, melting metal parts, powering sensors for monitoring and process control. Energy consumption varies widely depending on the process used and it is also unique for each type of machine used [5]. Some works in the literature compare the costs [1].[6] and the energy consumed [7] - [8] in relation to different 3D printing techniques employed. Zhang et al. [9] developed an additively constructed microchannel heat exchanger in Inconel 718. Compared to similar exchangers made for traditional manufacturing, this exchanger allows a 25% increase in efficiency concerning the exchange of energy. Romei et al. [10] proposed a tubular exchanger in 316L stainless steel resistant to high temperatures

for use in spacecraft, built with the SLM technique. Studies on the improvement of roughness in heat exchangers with micro-channels made with laser additive technology (Laser Bed Fusion) were done by Kirsh and Thole [11]. The manufacturing mechanism is reported in Fig.1.1. It consists in drawing the component on CAD software, converting it into STL format, and sending it to the machine. The latter creates the component following the CAD drawing layer by layer. Many techniques are available, which can be categorized according to their raw material (Powder, liquid, solid based). These are shown in figure 1.2.
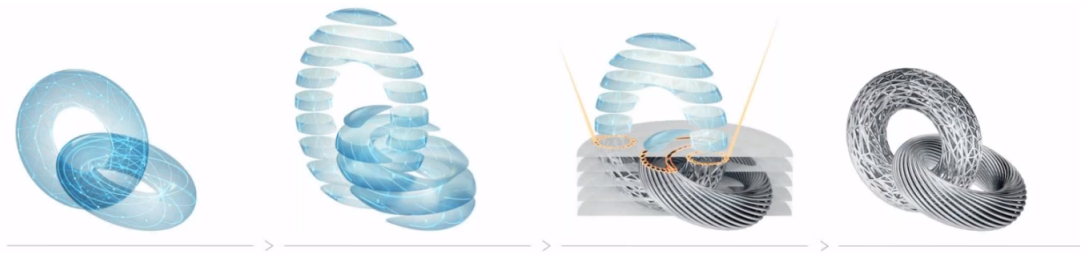
Figure 1.1: Additive Manufacturing process, from left : Creation of digital model, 2D discretization, Selective powder printing, final object(Reported from: eos.info)
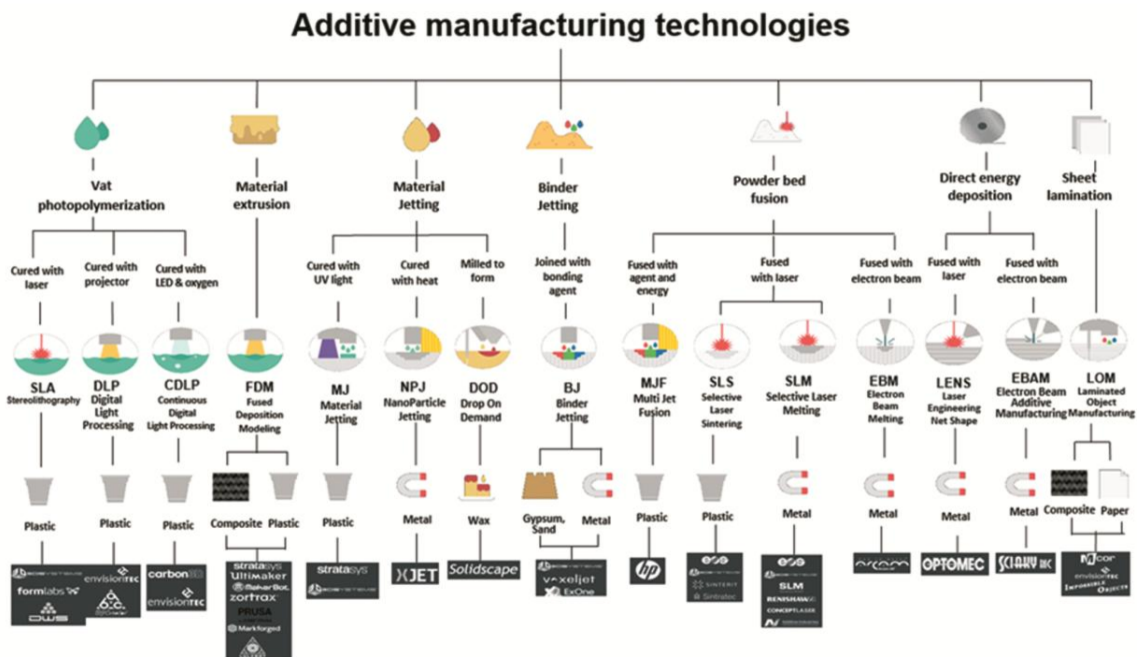
Figure 1.2: Additive Manufacturing technologies (Reported from: Additive manufacturing of composite materials by FDM technology: A review.)[12]

Like all technologies, in addition to the advantages, there are also limitations. Those of the AM are:

1. Slow Build rate

2. High production costs

3. Considerable effort required for application design and for setting process parameters

4. Manufacturing process

5. Limited component size

6. Low production volume

The sectors that have fully exploited this technology are mainly Automotive, Aerospace, and Biomedical. However, with the growing demand and available materials, sectors such as jewelry and hydraulic valves are also approaching the world of 3D printing. A sector that is still little explored but of great interest in this historical period is that relating to electrical applications. It is exciting both for research and from a commercial point of view to carry out a feasibility study for producing components such as transformers, rotors for electric motors, electromagnetic shields, and electromagnetic and electromechanical devices through Additive Manufacturing. The reason to combine additive manufacturing with the electrical sector is that today, the attention toward environmental sustainability has grown. The challenges to be overcome are of reducing harmful emissions and fighting pollution. Among the forms of pollution is the environmental one due to the exhaust gases of vehicles with internal combustion engines and to produce waste that must be disposed of correctly. A possible investigation solution is the realization of electric motors through 3D printing. This would allow for reduced production waste and new sustainable engines.

The combination of AM and finite element analysis and, in particular, topological optimization affects not only the creation of new geometries for these objects but improvements in performance with less waste of material and, therefore, less weight of the objects. Examples of electrical applications were studied by Tiismus et al [13] in which they present a comparison of the performance of a 3D printed transformer with the same traditionally manufactured object. Naseer et al. [14] as

well as Wrober et al. [15] presented a review on Additive Manufacturing possibility on electrical machines in wich the recent publications on AM of the active and passive part of the motor are presented. Fig 1.3 shows the results of these studies.
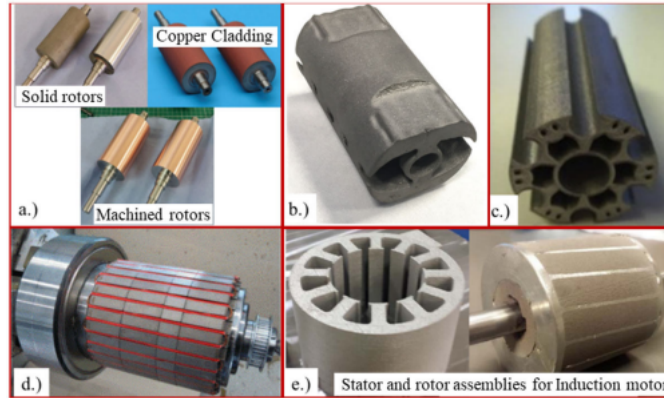
Figure 1.3: Examples of AM-built cores (Reported from: A Review on Additive Manufacturing Possibilities for Electrical Machines)[14]

1.1 Research Scope and Aim

Based on what has been said in this chapter, the purpose of this thesis is outlined. The applications studied mainly concern small electromagnetic shields, plug electromagnets, and transformers. The material used is a soft magnetic material, FeSi2.9, which was found to be a good candidate for AM fabrication using powder bed technology. The characteristics of this Fe-Si alloy are high electrical resistivity, helpful in reducing losses due to eddy currents that increase with increasing frequency, and excellent magnetic properties. The LPBF was preferred over EBM not only for economic and technical reasons but also because it reaches better resolutions and low surface roughness than EBM. This work aims to demonstrate the potential 3D printing of ferromagnetic materials for electrical applications. Some applications will be presented that will highlight the properties of printed pieces compared with the same products using traditional techniques. The innovations brought about by this research are many—first, the manufacture of components in soft magnetic material using additive technologies. Second, new applications are proposed concerning the rotors of electric machines already present in the literature.

1.1.1 Research Objectives

The goals of this research are the following :

1. Feasibility study to produce FeSi2.9 components through LPBF technique: Find the correct parameters that achieve the best materials properties concerning the target performance;

2. Comparison between the 3D printed components and the same fabricated through other methods, concerning the electromagnetic properties.

3. Investigate the possibility of improving the performance of the components through post-process treatments:

4. The magnetic properties of the 3D-printed material are integrated into the design process, and assess how both the design strategy and material properties affect the performance of the device as compared to the initial design.

5. Investigate conductive materials to print with LPBF technique;

Chapter 2

Additive Manufacturing

2.1 Introduction

This chapter proposes the potential of additive manufacturing as a manufacturing technology for electrical components. The first part is dedicated to an overview of the technologies currently on the market that use metallic materials. Technologies dealing with polymeric materials will be excluded from this discussion. Subsequently, the materials used for such applications (ferromagnetic and conductive) will be described. Finally, some applications presented in the literature will be reported. The study will allow us to conclude that the active parts of electric motors (rotors) and, for example, copper windings have a great potential to be printed using AM technology. The LPBF appears to be the best option to achieve this goal.

2.2 Additive Manufacturing Technologies

As mentioned in the introduction, AM has significant advantages. First of all, design freedom, thus giving the objects produced new functional geometries at no cost. In particular, it has been shown that using these technologies is advantageous in terms of production costs if the geometry of the pieces is very complex, as they would be costly if produced using traditional techniques. Since AM technologies only add material where needed, no production line and direct operator control are required. Figure 2.1 shows a graph representing the case in which it is convenient to use Additive Manufacturing. It is noted that for low production volumes, the

technology compares favorably with the traditional one. As the production volume grows, AM technologies are advantageous when the increased performance given by complex geometry is more important than the unit cost. Another benefit of AM is the simplification of the supply chain. Regarding the current obstacles to AM technology, we have low productivity compared to traditional production, high machine and raw material costs, and difficulty making AM components using traditional software. The workflow of all additive technologies can be divided into
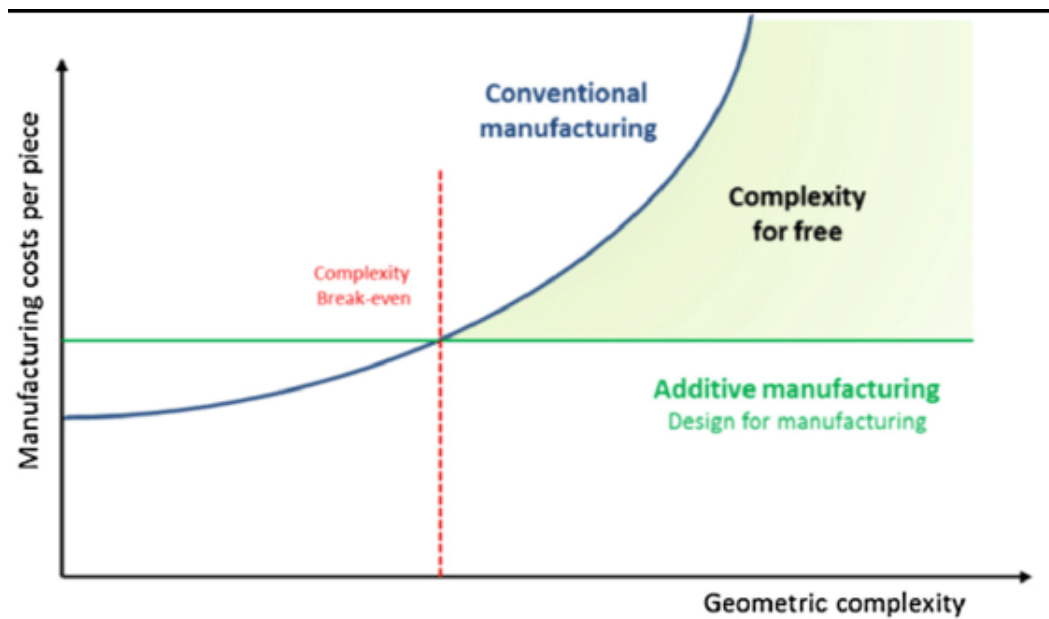
Figure 2.1: Complexity for free using additive manufacturing (Reported from: Why Education and Training in the Field of Additive Manufacturing is a Necessity)[16]

the following steps:

1. Creation of the object using CAD software. The topological optimization algorithms are implemented in this phase to improve the piece's structure.

2. Conversion of the CAD model into the Tessellation Standard Language format (.STL). The conversion foresees that the surface of the model is replaced with a triangular mesh in which a property is attributed to each node of the triangle. Once in the .STL format, the model has oriented in the AM build platform coordinate system. Support structures are introduced if there are cantilevered structures or to remove the piece more easily.

3. Loading the STL model into the machine. Once the STL model has been oriented, supported, and divided into various layers, it can be sent to the machine for production.

4. Setting of process parameters. The manufacturing process parameters, such as the power of the heat source, and speed, are set concerning the desired final properties of the constructed component (s), e.g., low surface roughness, low porosity, and many other constraints, such as productivity. Optimal parameters are generally unique to each material-manufacturing combination of platform and part geometry and should be determined through a phase of systematic optimization of the parameters;

5. Construction phase. The process is then started, and the part is created layer by layer, depositing dust or metal material (depending on the AM technology used), according to the correspondent CAD model;

6. Removing the component from the build platform. Once the "job" is completed, the part will be detached from the printing platform by removing the support structures;

7. Post-processing of the part. This last phase refers to many finishing procedures required for a part to become operational. These may include milling, polishing, thermal, and mechanical treatments.

Figure 2.2 shows the main commercially AM technique to produce metallic components. This chapter aims to show AM's potential for producing components for the electrical sector, such as rotors for the electric motor, ferromagnetic shields of electromagnetic fields, and copper windings. So only the processes that allow a high density and an acceptable roughness will be treated in detail. From the table, these are EBM, LPBF, and Binder Jet. The following sections will describe aspects of these processes and a comparison of the three.
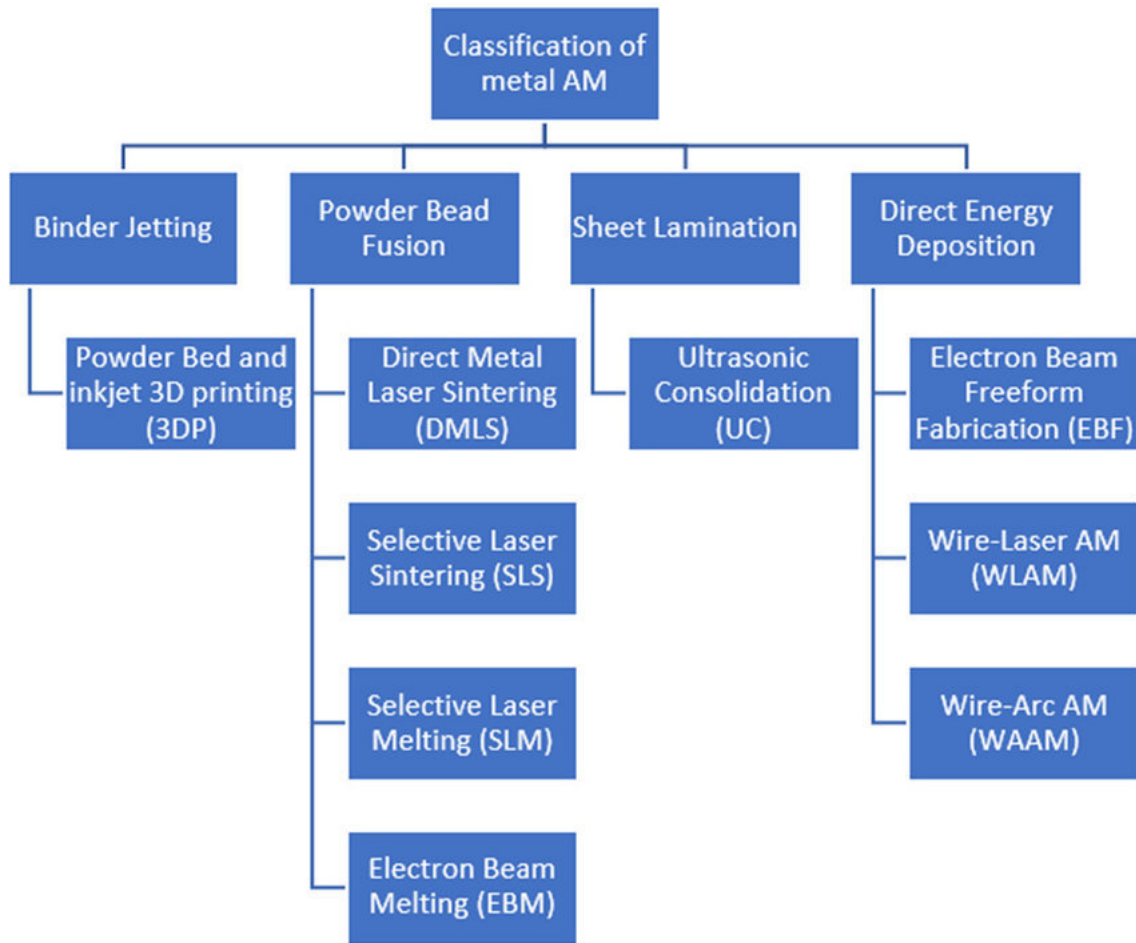
Figure 2.2: Classification of AM Technologies (Reported from: eview of Wire Arc Additive Manufacturing for 3D Metal Printing)[17]

2.2.1   EBM

Figure 2.3 shows the schematic of the Electron Beam Melting (EBM) process. The fabrication of the part happens in the build chamber. In order to not have gases inside it, the "job" is carried out in a vacuum. Typically, helium insufflation is done to avoid the electrical charging of the powder particles. The part is fabricated over a plate that is preheated prior to the start of the build. The preheating of the printing platform allows distension of the grains and eliminates residual stresses during the manufacturing process, reducing post-processing times. The peculiarity of the EBM process is the double scanning of the metal powder. In the first phase, the electron beam is passed with low power and high scanning speed to heat the
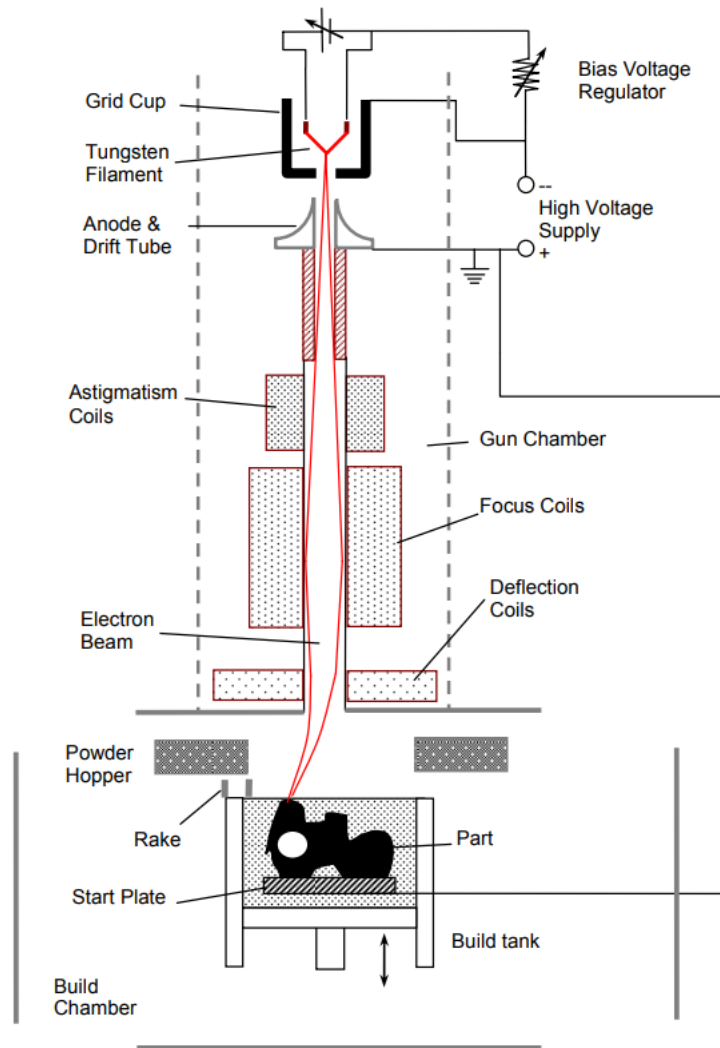
Figure 2.3: Schematic diagram of the EBM process (Reported from: Electron beam melting)[18]

powder. Then the power of the electron beam increases, and the scanning speed for powder melting decreases. The larger spot size of the electron beam compared to the laser in the LPBF causes greater roughness in pieces produced by EBM, as shown in figure 2.4.
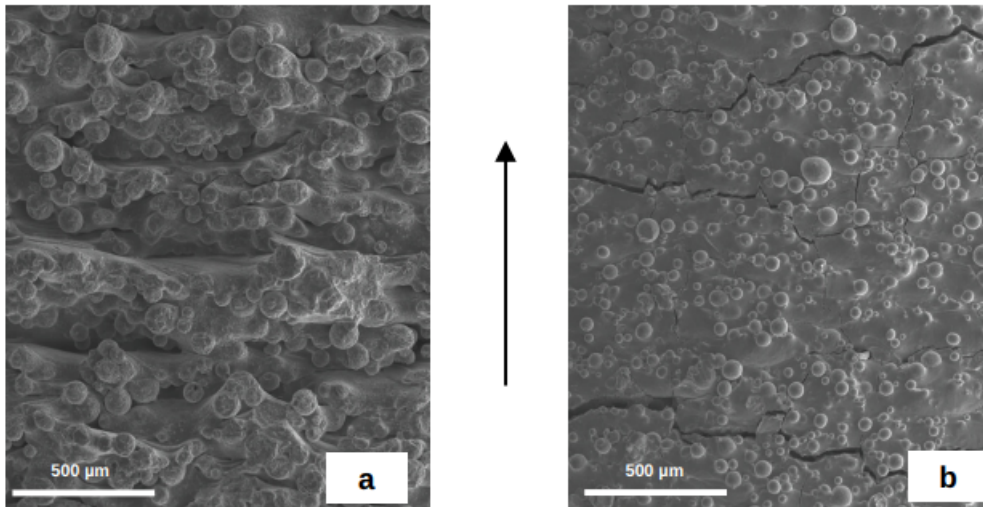
Figure 2.4: SEM picture of the surface of the specimens a) EBM, b) SLM (the arrow indicates the building direction) (Reported from: Comparison off Selective Laser and Electron Beam Melted Titanium Aluminides") [19]

2.2.2 LPBF
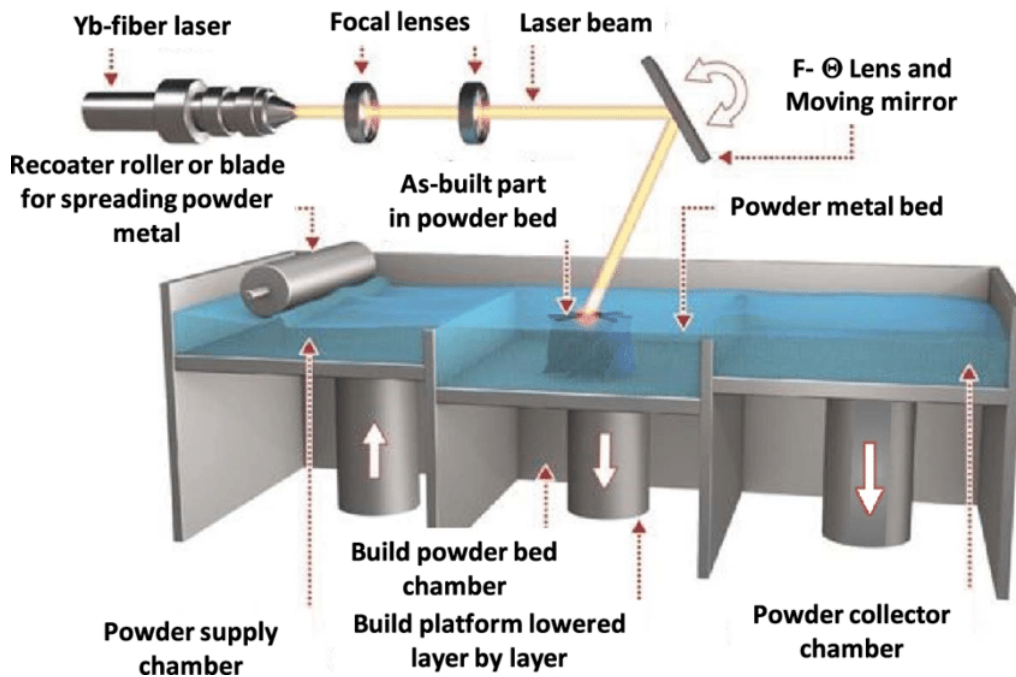
Figure 2.5: Laser Powder Bed Fusion Process (Reported from: Focus Variation Measurement and Prediction of Surface Texture Parameters Using Machine Learning in Laser Powder Bed Fusion)[20]

Figure 2.5 shows the LPBF manufacturing process. The working platform temperature is 1/5 of the EBM, around 100 ° C in this case. The powder is melted through a laser beam ranging from 100 to 1000W. The chamber is not vacuum-packed but works by blowing Argon or Nitrogen gas. The surface roughness is reduced compared to the EBM case, but the pieces require post-processing treatments to reduce residual stresses. The latter causes cracks in pieces produced if the machine parameters are not optimized. The reason why the productivity of the EBM machines is higher than the LPBF. However, since there is no double pass of the laser, the LPBF process is more practical, versatile, and less expensive

2.2.3 Binder-jet

It is an additive manufacturing method (AM) not based on the melting of the powder by laser or electron beams. The printing takes place through a jet of binder (BJ3DP), sprayed on the powder's various layers, selectively joining thanks to the densification process 2.6.
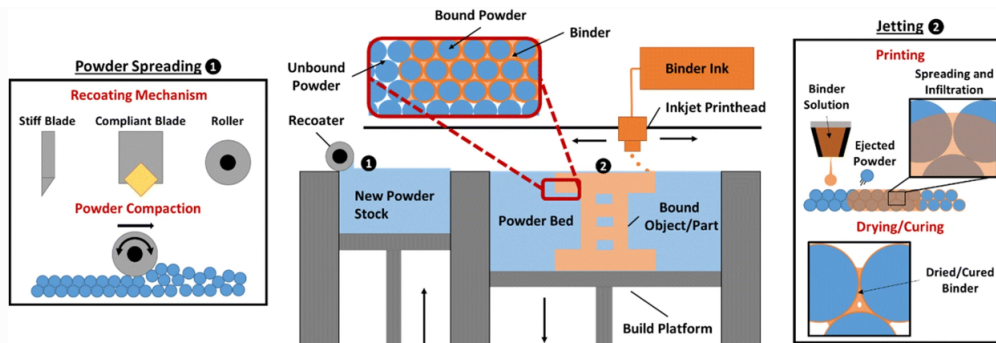
Figure 2.6: Schematic diagram of the Binder-Jetting process (Reported from: laboratory-scale binder jet additive manufacturing testbed for process exploration and material development)[21]

2.3 Physical Metallurgy of LPBF

The Laser Powder Bed Fusion (LPBF) is a manufacturing process that involves different metallurgical mechanisms being present phenomena of melting and rapid solidification, which determine the density of the material, the stress state, and the microstructure of the final piece. These mechanisms affect the functional behavior

13

of the finished product; therefore, it is necessary to describe them in this paragraph and the different machine parameters of the LPBF technique. The notions introduced in this chapter will lay the foundations for interpreting the behavior of the FeSi alloy processed by LPBF in the context of this research work. The metallurgical mechanisms that come into play in the additive manufacturing of powder bed metallic materials are:

- Melt-Pool and Pore Formation

- Residual Stress and Crack Formation

- Microstructure

A complete overview of the existing literature will describe each of these mechanisms in the following paragraphs.

2.3.1   Melt-Pool and Pore Formation

The manufacturing mechanism of the LPBF process consists of the melting through a laser source of the powder metal material to be processed. The interaction between laser and metal powder leads to different thermal phenomena. As described in [22], the area of the melting pool and the neighboring area affected by the heat generated by the pool are identified. A qualitative image of this interaction is shown in figure 2.7. During this interaction, certain phenomena may occur, such as:

1. **Spatter**: The expulsion of partially or melted particles from the melting pool. The material's surface is melted and, at times, vaporized into the plasma to help the material absorb the laser. Under the blow-off impulse pressure, the melted material is compressed to cause some liquid material to leave the molten pool at a certain speed, thereby forming the spatter as reported in figure 2.8
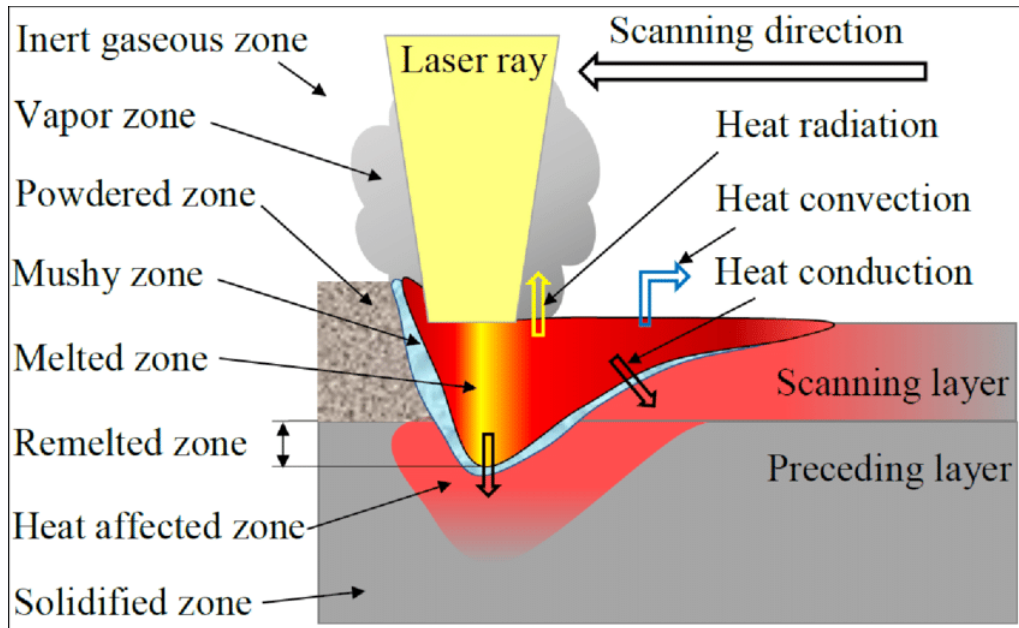
Figure 2.7: Scheme of melt-pool and heat-affected zone during LPBF process (Reported from: aser Polishing of Laser Powder Bed Fusion AlSi10Mg Parts—Influence of Initial Surface Roughness on Achievable Surface Quality)[23]
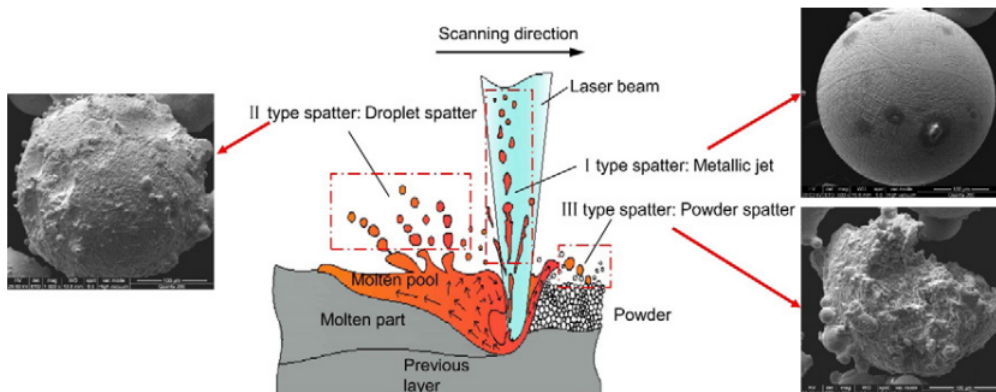
Figure 2.8: Formation mechanisms of different types of spatter: (a) morphology of spherical splashing (type-I splashing); (c) morphology of coarse spherical morphology (type-II splashing); (d) morphology of irregular splashing (type-III splashing).(Reported from: Mechanisms and characteristics of spatter generation in SLM processing and its effect on the properties) [24]

2. The condensation of the vapors of metal generated in the vicinity of the interaction zone laser-matter;

3. **Denudation**: The movement of unfused powders due to the action of the laser;

4. **Balling** : Surface tension, which concerns the spheroidization of the molten metal, figure 2.9.The surface tension can cause the phenomenon of Balling, preventing the molten material from binding to the underlying substrate and causing the onset of Plateau-Rayleigh instabilities that lead to the breakage of the molten track when the length-width ratio of the latter $\frac{l}{d}$ is higher than the viscosity of the liquid, as shown in Figure 2.10.
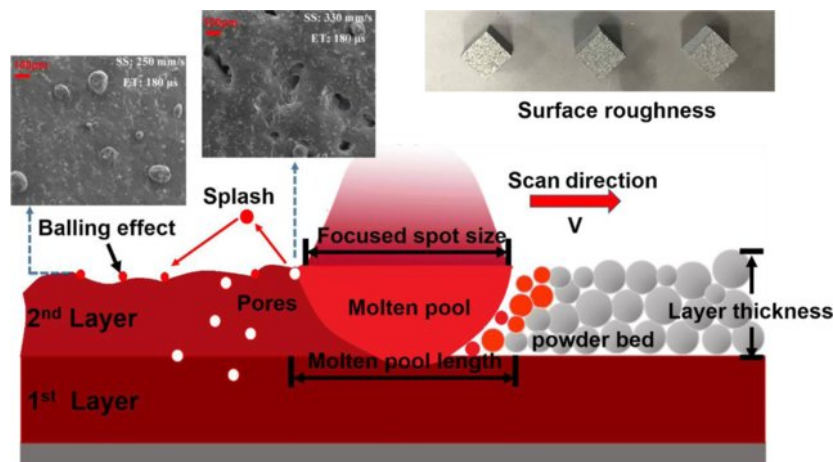
Figure 2.9: Balling effect caused by high laser power. (Reported from: A short review on selective laser melting of H13 steel) [25]

This leads unavoidably changes to the integrity of the powder bed, which after a complete process of LPBF can present agglomerates of particles, partially fused or oxidized particles partial / total, condensation of metal vapors and spatter [26]. Both powders move due to interaction with the laser (more or less accentuated) than metal vapors that they condense and spatter; they redeposit on the dust surrounding, going to modify locally some properties including surface morphology, chemical composition (including the possible formation of oxides), particle size and flowability [27]. This affects the entire bed fusion process dust, because the particles re-emitted from the melting zone and dispersed by the inert gas stream can be melted in successive layers or in the one still under construction and be so present in the manufactured piece; acting potentially as discontinuities and therefore preferential sites of nucleation of cracks, they can bring the mechanical properties of the

manufactured to be inferior (in some cases of fatigue life even dramatically lower) than those of metallic material free of such impurities [28].
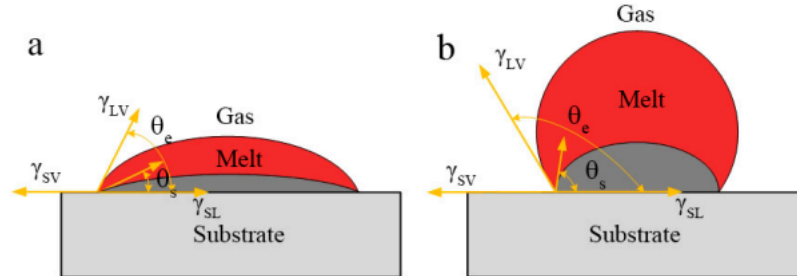
Figure 2.10: The schematic of liquid metal in the condition of (a) wetting and (b) non-wetting.(Reported from: alling Behavior of Selective Laser Melting (SLM) Magnesium Alloy)[29]

2.3.2 Residual Stress and Crack Formation

Residual stresses, defined as stresses of traction or compression to zero resulting without any external load being applied, either this is due to a force or a thermal gradient in a component that results in equilibrium. These generally arise during the component manufacturing process and occur in well-defined areas having their maximum close to the surface. [30] Such tensions are undesirable as they lower the elastic limit of the material resulting in thus undesired deformation of the component with consequent premature breakage. Tensions residual traction reduces the mechanical performance of the material, its resistance to fatigue and its corrosion resistance. However, residual stresses are not always harmful. The residual compressive stresses many times have beneficial effects on the material, since in the field elastic is added to the tensions generated in the points where the load is higher, reducing the value. [30] Residual stresses are divided into categories according to three main criteria: the cause which generates them, based on their order of magnitudes, or the method by which they are measured. The causes of residual stresses can be mechanical, thermal, or chemical. The mechanical causes are due to mechanical processes carried out on the component, such as plastic deformation processes, which produce uneven deformations on the piece. Thermal causes depend on heating cycles and uneven cooling or cooling at excessive speeds. Chemical causes are internal volume changes due to chemical reactions or precipitation and the transformation of secondary phases. [30]. Based on the order of

magnitude, their categorization is made in consideration of a parameter that takes the name of "characteristic length," which is the spatial dimension within which the internal stress state develops and balances itself. Based on this criterion, three are defined different types of residual stresses:

- First type: stresses that affect several crystalline regions of the material and originate especially following processes such as forging, rolling, finishing, or following thermal processes such as welding and heat treatments. They result from inhomogeneity between different crystalline regions with a fairly vast extension and develop on a scale macroscopic enough to be analyzed using traditional continuous models;

- Second type: tensions affecting a particular grain of the microscopic level material and almost always exist in polycrystalline materials as properties elastic and thermal vary between adjacent grains. This type of residual tension assumes significant value when the microstructure has more phases or when it occurs a phase transformation;

- Third type: stresses in which the characteristic length is less than the grain size Furthermore, we speak of stress on the nanoscale. They were tensions generated by internal inhomogeneities of the grain and which are balanced within it.

The residual stresses analyzed for which a solution is sought on the components produced by AM, they are those of the first type, as they develop on a macroscopic scale could compromise the surface and structural integrity of the parts. Tab 2.1 shows the most used measurement methods to evaluate residual stresses in AM: In order to perform an excellent product and process design, it is important know

Methods	Penetration	Resolution	Accuracy	Cost	
Hole drilling	Size of hole dia.	50-100μm depth	$\pm$50MPa	Low	
Curvature	0.1-0.5 of thickness	-	Minimum measurable	Medium	
X-ray diffraction	Near-surface	lateral. 20 μm depth	$\pm$20MPa	High	Neutron diffrction
Volumetric	500μm	$\pm$40 $\cdot$ 10^{-6} strain	High		

Table 2.1: Methods used for the evaluation of residual stresses in AM components

the distribution of residual stresses within the component as those of traction can change the static and dynamic properties of a material significantly. Their knowledge also allows us to optimize the parameters of the process and also in situations in which these are not avoidable, the knowledge of how they are generated and the influence of the parameters of processing allows you to evaluate the extent, minimize them and intervene with appropriate operations to reduce their effect during subsequent processing. The thermal cycle to which the components produced by LPBF are subjected is characterized by a localized heating in the area of the powder bed that will be selectively fused, with an energy intensity that allows having a temperature at least equal to the melting temperature of the alloy processed in the machine, which will be followed by rapid cooling and obtaining an area solidified. Moreover, the process involves the simultaneous melting of both the layer being processed both of the underlying layers have already previously solidified, thus creating its partial remelting subjecting it to a new thermal cycle. The residual stresses generated on the metal pieces processed are a significant problem, and excessive thermal gradients and residual stresses can cause component distortion both during the process, with part elevations and they can cause an imperfect spreading of the powder bed or damage to the recoater is a distortion of the final component that will not respect the tolerances geometric and dimensional requirements, as well as partly the desired mechanical characteristics. The main mechanisms of formation of residual stresses, which are often mentioned in the literature, are the TGM (Temperature gradient mechanism) and the cooling phase model (cool-down phase model) [31]. The TGM model states that, during the heating phase, the source, which provides a high energy intensity to ensure the melting, quickly heats the processed material that, due to thermal expansion, tends to expand. However, its expansion is hindered by the surrounding material at a lower temperature. This phenomenon creates compression tensions in areas that have undergone the thermal process. Once the energy source and, therefore, during their cooling phase, the heat-treated areas begin to cool, thus causing a localized shrinkage of the material partially contained by the plastic deformation generated during the heating phase. In this way, residual tensile stress is generated in the areas that have undergone the thermal process, balanced by areas with compression stresses. The second model, on the other hand, mainly deals with the mechanism of formation of residual stresses in metallic AM processes, due to the process of making the component layer after layer; in fact, for this reason, the previously melted material undergoes

due to the drafting of the next layer, a new cycle of melting and solidification. The cooling to which the material after re-solidification leads to its shrinkage, which is partially contained by the layer of previously deposited material, thus creating a state in the newly created layer tensile stress. The following figure 2.11 graphically illustrates the TGM model described above :
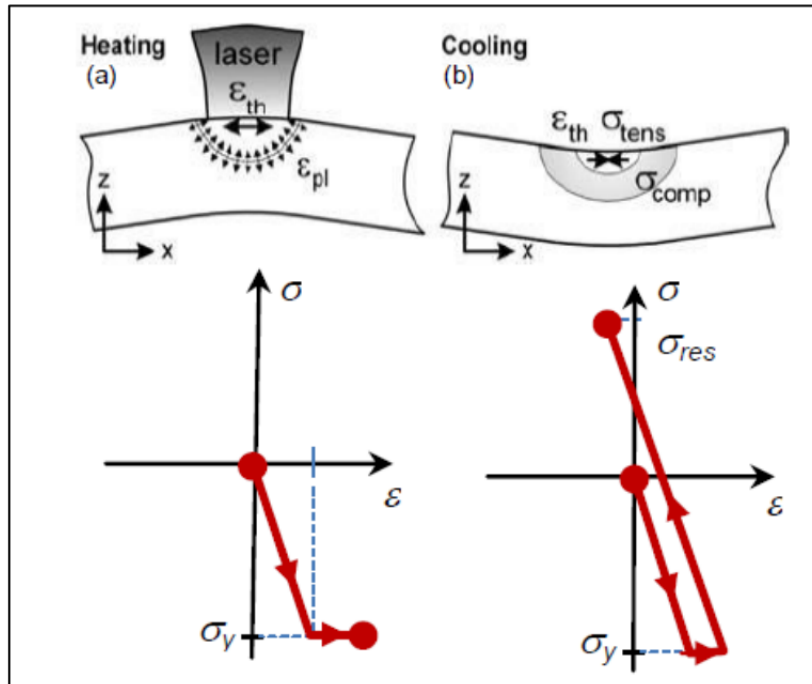
Figure 2.11: Residual stress formation model: (a) heating, (b) cooling. (Reported from: Residual stress analysis of additive manufacturing of metal- lic parts using ultrasonic waves: State of the art review)[32]

Although the models proposed in the literature give a valuable description of the phenomenon for understanding the birth of residual tensions, in reality, the problem becomes in the SLM more complex as the energy sources can be more than one, the configuration of the path of the energy source and the heat transfer between the melting point and the surrounding material can be quite complex [33]. The residual stresses in a component produced by SLM are highly dependent on parameters such as exposure strategy, laser power, and scan speed, but also by other factors, such as the component's orientation in the machine. As for the exposure strategy Kruth et al. [34] studied its effects on distortion e deformation of the components produced and saw that using an exposure strategy to islands (figure 2.12) allows reducing the distortion of the pieces produced compared to others types such as continuous or rotating the scanning angle between one layer and the next. Usually, different
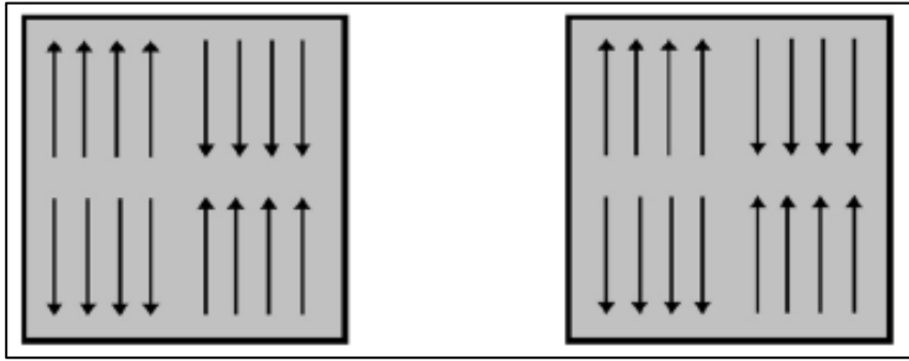
Figure 2.12: Example of a rotating island exposure strategy (Reported from: Scanning strategy in selective laser melting (SLM): a re- view)[35].

materials have in the as-built conditions the maximum residual stresses of traction along the construction direction (Z axis) just below the top surface, followed by areas where residual stresses become compressive in the core of the piece, and again traction in the lower surface [31]. The variation in the number of residual stresses in the component can also be linked to the energy density supplied to a specific area. The energy density varies from technique to technique since these require different input parameters. Another important parameter for construction optimization that affects the residual stress is the hatch distance. Sochalski-Kolbus et al. [36] have demonstrated the residual stresses are greater in the regions where there is an overlap of the wells of a merger as a recast takes place in these areas.

2.3.3 Microstructure

The microstructure of a component made by additive manufacturing is distinguished by proper microstructure and surface morphology. The solidification microstructure is the key to analyzing the properties and mechanics of a component made by additive manufacturing. The laser provides high energy and therefore induces very rapid heating, the fusion of the powder, and inevitably also rapid solidification due to rapid cooling. The cooling rates are of the order of 103 - 108 $\frac{K}{s}$ [37]. The presence of melt pools usually characterizes the microstructure and arched structures of small dimensions (≤ 1 mm) [38]. Instead of the conventional solidification, dendritic structures typical of ferrous alloys, a cellular and directional microstructure develops, devoid of secondary dendrites, as shown in Figure 2.13 a and Figure 2.13 [39] for the 316L powder treated with laser sintering (LS) and laser metal, respectively deposition (LMD) and in Figure 2.13 c for the laser-processed Fe-Ni-Cu-FeP alloy laser melting (LM) [40].
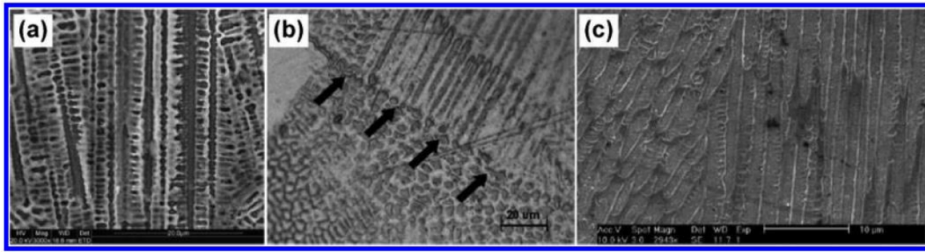
Figure 2.13: Example of a rotating island exposure strategy. (Reported from: Scanning strategy in selective laser melting (SLM): a re- view)[35].

The gradients of the chemical concentration and temperature of the melt pool cause a surface tension gradient, and the convection phenomenon of Marangoni [41], from which a non-equilibrium solidification process follows. Processes with rapid solidification are kinetically limited by the crystals, which increase according to the direction of maximum thermal flow. The action simultaneous but antagonistic to the two previous mechanisms, namely the solidification of non-equilibrium against the tendency to directional growth localized; it can cause different crystallographic directions, locally regular [42]. Therefore metal materials processed with additive manufacturing they can have intrinsic anisotropic characteristics. Another essential characteristic intrinsic to the components processed with additive manufacturing is the microstructure change along the deposition direction. In a study by Hofmeister

et al. [38], the variation of the cell dimensions of the alloys 316L and H13 treated with laser deposition of metals was analyzed. The different thermal cycles undergone by the various layers are the reason for the microstructure variation along the component's height, depending on the change in conduction, convection, and radiation conditions. The process parameters strongly condition the microstructural characteristics of a piece made by additive manufacturing. High temperatures are maintained for a long time, with high specific energy and a high material deposition rate (deposition rate/material addition rate); therefore, local temperature gradients are limited. In this case, the grains are coarse and equiaxed in shape. Conversely, a fine microstructure is formed with lower specific energies and deposition rates. Low specific energy is obtained with a high laser advancement speed. In this case, the profile of the melt pools narrows, the local temperature gradients increase along the entire layer, and in most of the components, columnar grains form.

2.4 Effect of L-PBF Process Parameters on Build Quality, Microstructures and Functional Behaviour

Additive manufacturing is a flexible and complex process even after many parameters are involved. Studies involving selective laser melting or powder bed fusion usually set some parameters and then analyze the mechanical and microstructural properties as a function of the parameters variables. Figure 2.14 lists some of the primary process parameters and materials properties essential to the success of the LPBF process.

Among the listed parameters, only the most relevant ones will be described, which are normally subject to optimization. These are represented in figure 2.15 and are:

- Laser Power;

- Beam Size;

- Scanning Speed;

- Scan Hatch Spacing;

LPBF Processing Parameters	Materials Characteristics
Type of commercial equipment	Particle morphology
Laser type	Particle size and distribution
Laser power	Chemical composition
Scan speed	Absorptivity (or reflectivity)
Scan radius	Melting temperature
Scan Hatch spacing	Specific heat
Scan vector length	Thermal conductivity
Layer thickness	Viscosity
Processing environment	Surface tension
Gas flow	Emissivity
Heaters (bed temperature)	Component ratio
Scan strategy	Boiling point

Figure 2.14: LPBF process parameters and material properties influencing the processing and densification [43].
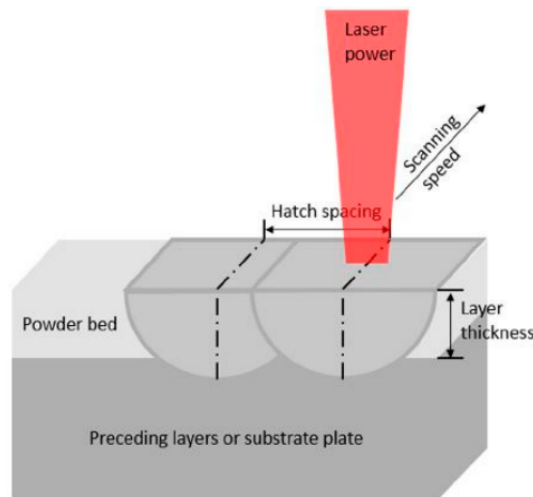
Figure 2.15: LPBF process parameters: laser power, scanning speed, hatch spacing, and layer thickness.(Reported from: Laser Powder Bed Fusion of Potential Superalloys: A Review) [43].

- Powder Layer Thickness;

The heat generated by the laser source to melt the powder spreads inwards. For this heat to be sufficient to bond the next layer to the previous one, a suitable combination of laser power and scanning speed must be found. This combination ensures that there is thus sufficient energy density to bind the dust particles together. If this is not achieved, the result is that of a partial melting which culminates in poor densification of the piece. High laser energy values for low scanning speeds increase

energy to the powder bed, causing a considerable temperature increase which involves the presence of a liquid phase of the material. Appropriate increments of the laser energy input lead to a high working temperature, which ultimately reduces viscosity and surface tensions [44]. In addition, the high working temperature promotes material transport thanks to the development of convective flows inside the molten bath during the laser sintering process. This reduces the size and number of inter-agglomerated pores, thus obtaining completely dense components. According to Olakami et al. [45], at low scanning speeds with relatively high laser power, there exists an optimum laser energy density at which the wettability of the liquid-solid is more successful, so that the particles in the liquid are rearranged more appropriately to achieve greater density. The increase in laser energy density after optimum leads to a decrease in the sintering density. In this condition, an increase in laser power increases the amount of liquid phase. However, the reduced scanning speed can result in extensive material evaporation and the keyhole effect [46]. Similarly, Yuan et al. [47] showed that there is a scanning speed threshold beyond which the density of the materials also tends to decrease. A combination of low laser power, high scanning speeds, and large layer thickness usually also culminate in insufficient energy [45]. This is because, in this condition, the laser energy produced is low, and the high scanning speeds lead to reduced interaction times. Therefore, under high scanning speed and low laser power, the size of the molten pool formed will be too small, limiting the contact area between the molten pool and the substrate. This leads to a lack of wetting, creep, diffusion, and balling characteristics. [48] The use of higher laser power and scanning speed increases the efficiency of LPBF processes. As the scanning speed of the beam increases, the heat loss by conduction decreases, and the energy of the absorbed laser radiation goes directly into the melting of the material [49]. Hence, the width of the scanned traces is comparable to the diameter of the laser beam [50]. Poor spacing between scan layers often results in regular porosity in the built parts. Pores typically start at the single layer level, and two scan tracks are distant [51]. They can be eliminated by overlapping them appropriately. Increasing the overlap of the scans reduces the depth of the melt or penetration pool which leads to less adhesion between the layers.

2.5 Effect of Laser Scanning Strategy on the Densification Mechanism

A scanning strategy is a way to build pieces by varying the orientation of the laser. The scanning strategy affects the thermal properties of the piece under construction. A correct scanning strategy choice allows the desired microstructure properties with a reduced presence of pores or internal cracks. Su et al. [52] investigated the influence of four different scanning strategies (Figure 2.16) on component construction [53]. The four scan patterns differ in build duration, deposited
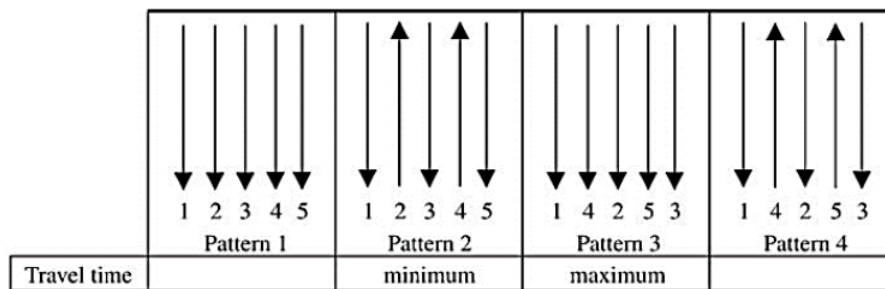
Figure 2.16: Four different scanning strategies. (Reported from: canning strategy in selective laser melting (SLM): a review)[35].

layer thickness, and surface characteristics. Strategy 3 allows obtaining a deposited layer more significant than the others. Furthermore, strategies 1 and 2 also have unwanted surface irregularities. Other authors have experimented with standard, diagonal, and perimeter strategies, as shown in the figure 2.17. The first two strategies gave good results in uniform layering, while the last strategy was less successful with distortions during construction. Another laser scanning strategy employed is the "island" one [54],[55],[56]. In this strategy, the geometry is divided into squares that form a checkerboard (figure 2.18). Each of the squares ("islands") is then selectively fused randomly. Within each of the "islands," simple scan vectors are used, alternating with of the main parameters, which are the "scan spacing" and the "scan speed." The "island" technique reduces the residual stresses inside the final component. The problem linked to this strategy lies in pores between the various "islands," so post-process heat treatments are required to reduce these defects.
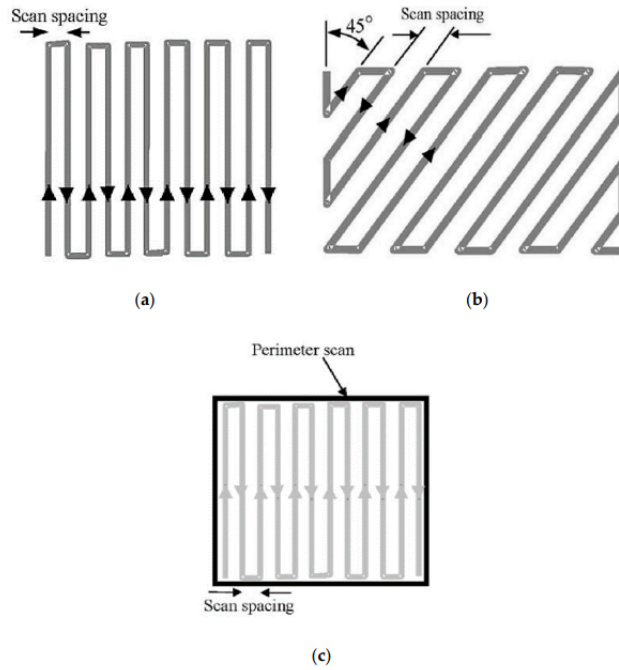
Figure 2.17: LPBF scanning strategies: (a) standard, (b) diagonal and (c) perimeter (Reported from: Laser Powder Bed Fusion of Potential Superalloys: A Review) [43].
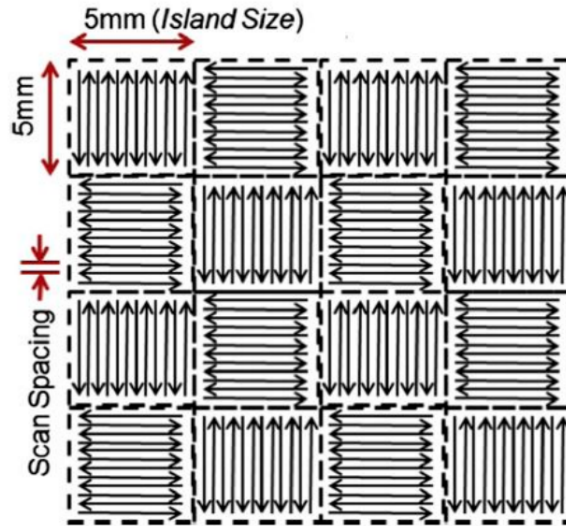
Figure 2.18: Schematic representation of the "island" scan strategy (Reported from: Laser Powder Bed Fusion of Potential Superalloys: A Review)[43].

Chapter 3

Ferromagnetic material for AM

The demand for next-generation, high-performance magnetic materials has risen significantly with growing interest in electrification. Electrical machine design for these applications faces challenges for the next generation of lightweight, ultra-efficient electric machines. Additive manufacturing (AM) opens up new improvements for the industrial manufacturing of electrical machines. The magnetic, electrical, thermal, and mechanical properties of the magnetic materials are also greatly influenced by the type of the AM method. With the ongoing evolutions, new components will be produced using this technology as an alternative to the traditional process. Similarly, in soft magnetic materials manufacturing, AM can provide the design freedom to control physical properties. For example, AM can open up the possibility of using various lamination thicknesses in electrical cores, teeth, and yokes [57]. Similarly, AM can not only provide the net-shaping of complex machine parts but also can facilitate the processing of higher quality alloys. Babuska et al. [58] recently reported improvements in tensile strength and ductility in additively manufactured Fe–Co alloy. AM has shown a more significant potential than conventional manufacturing to improve the functionalities of manufactured parts and components in various applications such as medical, aerospace, and electrical industries. The AM process for an electric machine core begins with generating a prototype model using CAD software and implementing the 3D printing using feedstock materials. AM is continuously evolving with the advancement of printing technologies; however, because of the necessity of the use of hard and soft magnetic materials in electrical machines along with copper wire insertion, a single-step fabrication of electrical machines is still a challenging future goal. Because AM can

enable easy printing of thin-walled hollow structures of new materials with high electrical resistivity, it offers excellent potential for core loss reduction. Even complex core designs can be realized; for example, continuous skewing and complex flux paths with integrated cooling channels can result in better-performing designs with substantial cost and weight savings and reduced waste of critical materials. Because AM allows a mix of different types of metal powders, higher-quality alloys, and the inclusion of binding agents, improved material properties are possible by controlling grain texture and the grade of soft magnetic materials in specific sections of the machine parts [59].

3.1 Fe-Si alloys: Metallurgy, Magnetic Properties and Manufacturing Processes

Silicon steels are one of the most important classes among materials for magnetic applications [60]. Among these, alloys with Si content between 2.0% and 7.0% by weight [61] guarantee excellent electromagnetic properties [62], such as to allow their use in electric motors, generators and transformer cores [63]. Adding a small percentage of Si leads to significant changes in iron's physical, mechanical and magnetic properties. The most relevant effect concerns the electrical resistivity, which increases by a rate of around $5 \times 10\text{-}8$ Ωm per percentage of solute. This generates significant benefits in terms of reducing AC losses. The main factors that limit the addition of Si are the reduction of saturation magnetization. The heterogeneous formation of Fe-Si in ordered phases involves, in fact, severe embrittlement of the material. The trends of the saturation induction and the elasticity limit for the Si concentration are shown in the figure 3.1
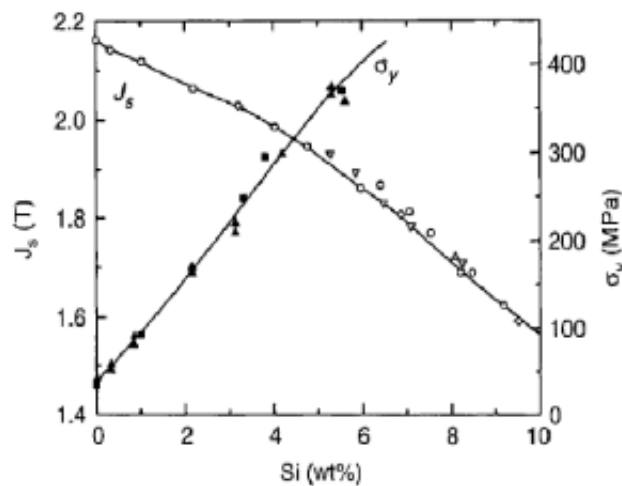
Figure 3.1: Saturation polarization and elasticity limit as a function of Si concentration in Fe-Si alloys (Reported from: Metallurgy of high-silicon steel parts produced using Selective Laser Melting) [60].

These alloys are used for transformer cores and are known as electrical steels. In the power industry electrical voltage is almost always AC and at a low frequency, 50-60Hz. At these frequencies, eddy currents are generated in the transformer core. Alloying the Fe with Si has a sizeable marked effect on the material's electrical

resistivity, with an increase of a factor of 4 for 3wt%Si. Silicon also has the benefit of reducing magnetostriction (i.e., length change on magnetization) and the magnetocrystalline anisotropy. The addition of too much silicon makes the material extremely brittle and difficult to produce, giving a practical limitation of 4wt% to the amount of Si that can be added. Typically most electrical steels will contain between 3 and 4 wt% Si. For transformer applications, the flux lies predominantly in the length of the laminations; therefore, it is desirable to enhance the permeability in this direction. This is achieved by various hot and cold rolling stages to produce textured sheets, known as grain-oriented silicon-steel, with [001] the direction in the length of the lamination. The <001> type crystal directions are the easy directions of magnetization; hence, the permeability is greater. Figure 3.2
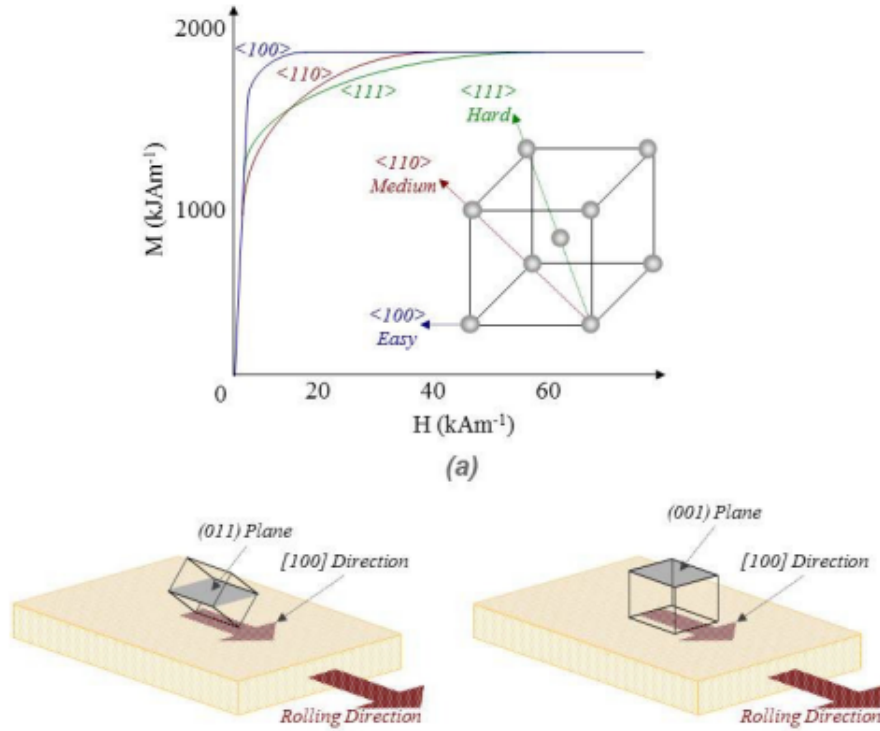
Figure 3.2: The anisotropy of Fe and types of texture that can be achieved (Reported from: Metallurgy of high-silicon steel parts produced using Selective Laser Melting) [60].

It has been amply demonstrated that an alloy with 6.5% in weight of silicon offers excellent magnetic properties ([64], [65]) such as high magnetic saturation,

32

low magnetocrystalline anisotropy, low magnetostriction and high electrical resistivity ([63],[66]). However,alloys with Si content between 3.5-4.0% ([58]) are more common. Alloys with high Si (Si content ≥4.5%) are intrinsically brittle and make it difficult to manufacture magnetic components through conventional processes ([65],[67]). The progressive embrittlement of the FeSi alloy increases the Si content and it is associated with the tendency to form phases sorted during cooling [68]. The FeSi alloy has a crystalline structure of body-centered cubic type (ccc); this, in the solidification phase, undergoes a rearrangement of the Si atoms in the Fe matrix, forming two types of ordered structures, B2 and DO3 ([69]). The movement of dislocations in an ordered structure is known to create anti-phase edges ([70]) increasing the energy of the alloy and strengthening the same. Likewise, the presence of ordered structures reduces the alloy's ductility and limits its mechanical workability at low temperatures. Some fundamental properties will be described in this chapter in order to correlate the physical properties with the process parameters and the related microstructure. This description will allow us to understand better the properties deriving from the production of FeSi2.9 through LPBF

3.2 Metallurgy Effects on the Magnetic Properties of Fe-Si Soft Magnets

The phase diagram of the Fe-Si alloy is represented in figure 3.3. The system is body-centered cubic for a percentage of silicon greater than 2% (BBC).

The characteristic of this material, as well as all soft magnetic materials, is to become magnetized when an external magnetic field is applied. This behavior occurs because the domains align parallel to the applied magnetic field. As soon as the external excitation is turned off, the domains return to their initial zero energy condition. In nature, there are different crystallographic directions that bring different properties to the material. The various crystallographic directions are shown in the figure 3.4

Three fundamental directions can be distinguished, easy, medium, and hard magnetization. Respectively the magnetic moments of each magnetic domain will be aligned along the direction of the magnetic field at 0, 90 degrees, and 180 degrees. The movement of the domains is opposed by defects in the microstructure that exert an opposite force to their movement. The force applied is proportional to the size
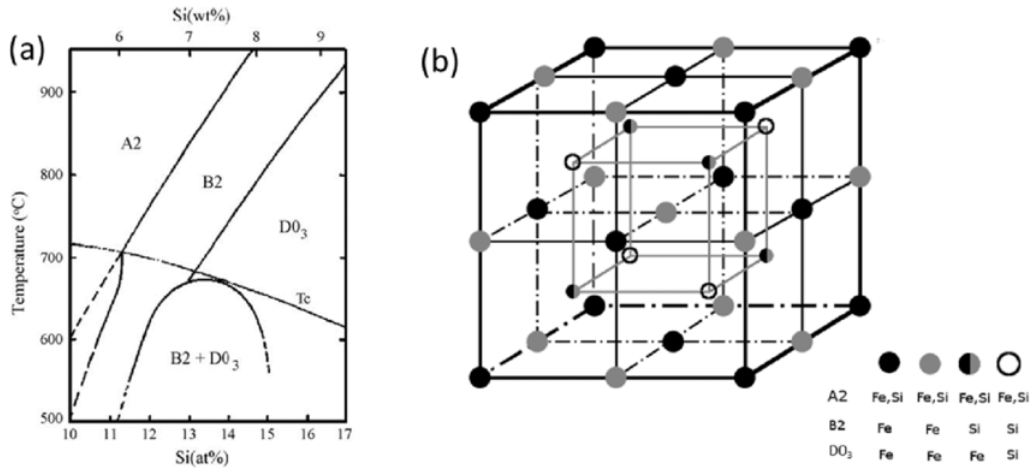
Figure 3.3: Phase diagram FeSi (left) atomic structure (right). (Reported from: Review of Fe-6.5wt%Si high silicon steel—A promising soft magnetic material for sub-kHz application) [66]
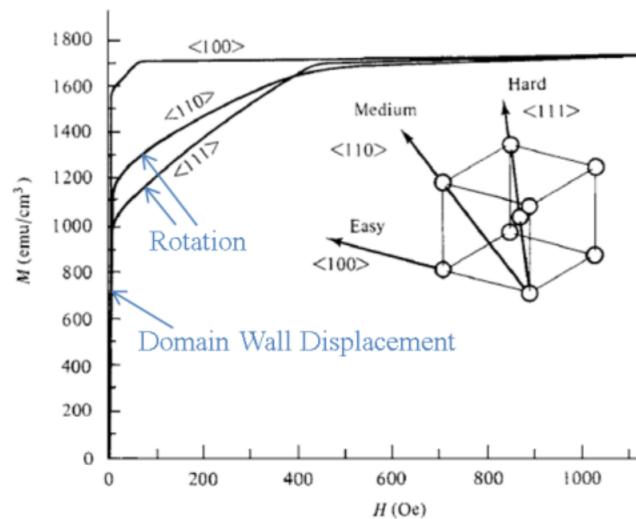
Figure 3.4: Phase diagram FeSi (left) atomic structure (right) (Reported from: Review of Fe-6.5wt%Si high silicon steel—A promising soft magnetic material for sub-kHz application) [66]

of the defects and is maximum when the defect is of the same order of magnitude as the domain walls. The primary defects that can be found are:

- stress centres;

- grain boundaries;

34

- point and line defects;

- precipitates, porosities

From this, it follows that the sum of three contributions describes the coercive magnetic field:

$$H_c = H_{co} + H_{cg} + H_{ci} \tag{3.1}$$

Where:

- H_{co} :contribution residual stress;

- H_{cg} :contribution grain boundaries;

- H_{ci}:contribution of non-magnetic inclusions;

The characteristic hysteresis curve of ferromagnetic materials is S-shaped, as shown in figure **??** composed of the low value of remanence and coercitivity. When described in equation 3.1, this implies that the components must be dense and have few defects. The area inside the cycle represents the energy lost, so the smaller it is, the less the losses will be.

Total losses in ferromagnetic materials consist of hysteresis losses and eddy current losses. Figure 3.5 shows the trend of losses as the grain size varies. The graph shows that the hysteresis losses are high for small grain sizes. As the size increases, the total losses decrease until there is a trend reversal compromising the efficiency of the material. For frequencies around 50 Hz, the grain sizes must not exceed 5-7 mm, while for frequencies higher than 400 Hz, the grains must have dimensions below 100 micrometers. One of the challenges to be overcome is to guarantee the same properties in every direction of the component
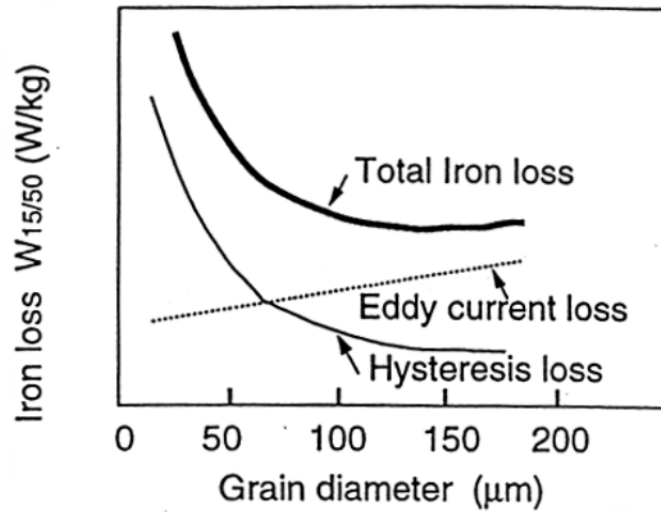
Figure 3.5: Total loss variation with grain size (Reported from: Annealing of electrical steel)[71]

3.3 Effects of %Si on Fe Properties

In this paragraph, the percentage by weight of silicon is described to optimize the magnetic properties of the final alloy represented by saturation magnetization, total losses, maximum permeability, coercivity, and hysteresis losses. In figure 3.6, it is highlighted how all the other properties increase with the increase of the Silicon content except for the magnetization at saturation. In particular, the best percentage from the point of view of losses is around 6.5%. The positive effects of the high silicon content are given by the increase that the last places on the electrical resistivity. Although the magnetic properties improve, the mechanical ones deteriorate. The yield and tensile strengths fig.3.7 increase until 4.5% after that, they begin to deteriorate. This alloy is challenging to work on because of the high ductility for a percentage of silicon higher than 5%. For this reason, most of the FeSi alloys are composed of a percentage of Si lower than 3.5%.
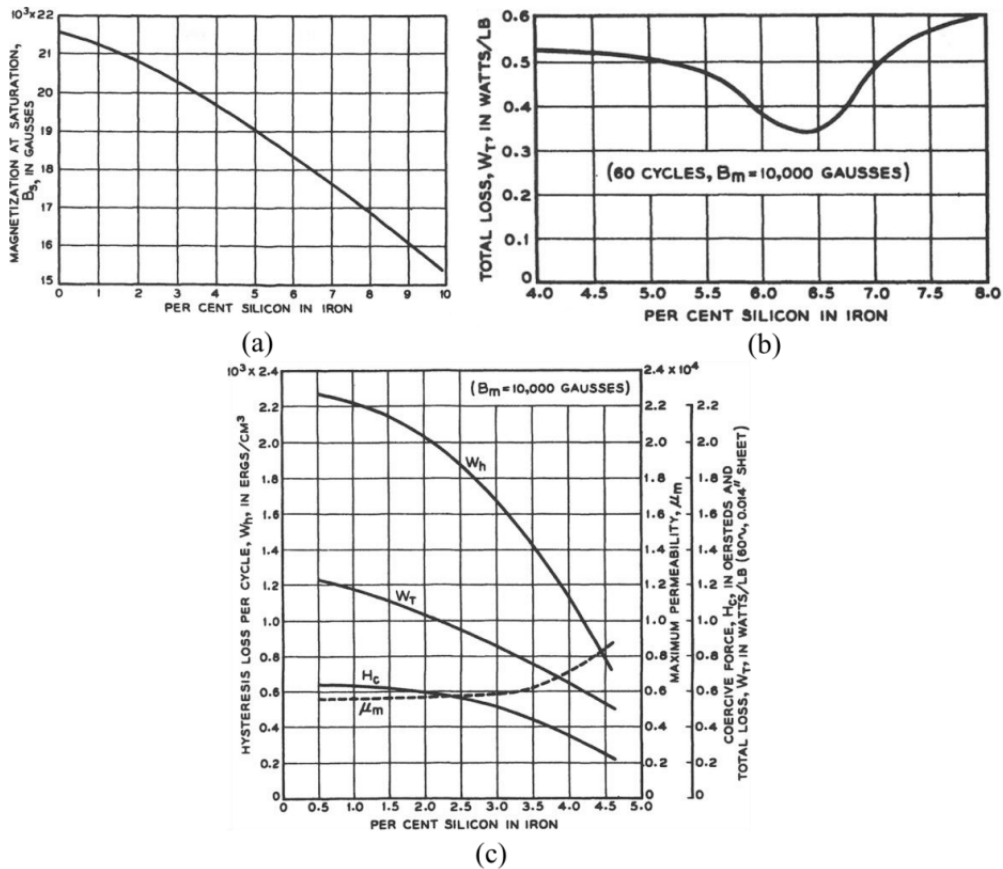
Figure 3.6: Effect of Si content on magnetic properties of Fe (Reported from: Metallurgy of high-silicon steel parts produced using Selective Laser Melting)

3.4   Losses in magnetic materials

When subjected to an alternating magnetic field originating from alternating currents, in ferromagnetic materials, there are energy dissipations due to the irreversibility of the material's magnetic domains. The two main phenomena that oversee this loss of power are:

- Magnetic hysteresis;

- Eddy currents

The power losses caused by the magnetic hysteresis are directly related to the energy expended in the volume unit of material so that it completes a complete magnetization cycle. The specific losses due to magnetic hysteresis $P_i(W/kg)$ are

37
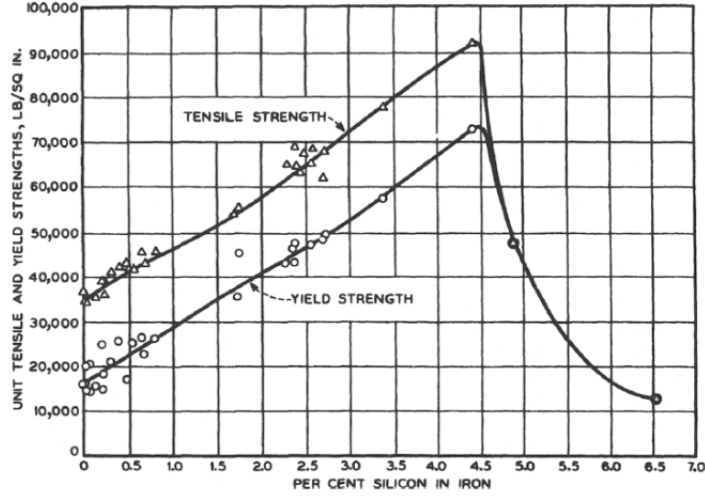
Figure 3.7: Effect of Si content on the mechanical properties of Fe-Si(Reported from: Metallurgy of high-silicon steel parts produced using Selective Laser Melting)

expressed as follows:

$$P_i = K_i \cdot B^{\eta} \cdot f \tag{3.2}$$

The direct proportionality with the excitation current frequency, generating the magnetic field that varies over time, is highlighted. The approach to limit this loss contribution is essential to opt for a material with the hysteresis cycle as narrow as possible: we are talking about the material with a homogeneous structure, very high purity, and modest internal stresses. Elements such as silicon, phosphorus, and aluminum, are commonly added in alloy to iron to meet the prerequisites mentioned above.

The second contribution (the power losses due to eddy currents) is because, in a ferromagnetic material, a time-varying flux induces, according to Lenz's law, an electromotive force (f.e.m.). The latter tends, moment by moment, to counteract the variation of magnetic flux. In the sinusoidal regime, it is proportional to the pulsation ω of the variable magnetic flux, therefore to the frequency and amplitude of oscillation and the magnetic induction B.

$$fem \propto \omega B \tag{3.3}$$

In Figure 3.8, there is a schematic representation of the phenomenon. The ferromagnetic material, being electrically conductive, is the seat of circulation currents,

generated by the f.e.m. induced, which have their closed paths on planes perpendicular to the magnetic flux.
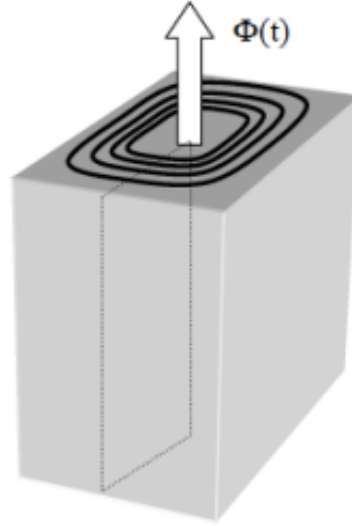
Figure 3.8: Eddy current circuits (black lines) within a massive ferromagnetic material

These eddy currents, which are limited by the ohmic resistance offered by the material, cause a power loss contribution due to the Joule effect, which can be expressed as follows:

$$P_{ec} = \frac{fem^2}{R_{eq}} \propto \frac{\omega^2 B^2}{R_{eq}} \tag{3.4}$$

Chapter 4

Experimental Methods for the Laser Powder Bed Fusion of Silicon Iron

4.1 Introduction

This paragraph describes the methodology adopted for the realization and characterization of the iron-silicon components produced by the LPBF technique. A description of the LPBF system used, the raw material, and the samples produced for the print characterization is provided. Subsequently, the printing strategies studied to obtain a density close to 100 % and the thermal treatments for the relaxation of the grains will be illustrated. Finally, the samples and techniques used for magnetic characterization will be described.

4.2 Description of the L-PBF

Samples for magnetic characterization were manufactured with a LPBF system with open architecture (figure 4.1. The system is equipped with a fiber laser source (Corona nLIGHT AFX 1000, nLIGHT Inc, Vancouver, Washington, USA), operating with a wavelength of 1070 nm ($\pm$10 nm), maximum power of 1000W, and a theoretical waist diameter of 47 µm in the focus position. The laser source can operate either in Pulsed Wave (PW) or Continuous Wave (CW) emission by power modulation. Before manufacturing, the building chamber is filled with Ar.

Throughout the experimental activity, ferromagnetic samples were built upon stainless steel substrates.
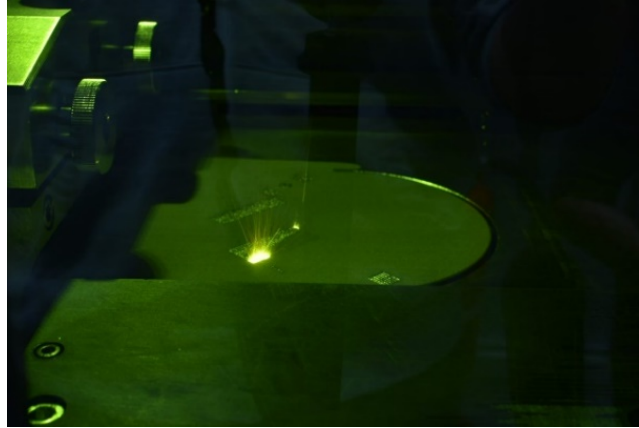
Figure 4.1: LPBF System

4.3 Fe-Si2.9% Powder

The Fe-Si2.9% Powder was utilized for its electromechanical applications. Although a greater quantity of silicon increases electrical resistivity and therefore improves the losses of the components, as a first investigation, it was decided to proceed with an alloy with a low silicon content Fig 4.2. The powder in question is available on the commercial market, representing a significant advantage from an industrial point of view. The sphericity of the acquired powders was checked through a scanning electron microscope (SEM). Before its use, drying was carried out to eliminate the humidity present. This step improves flowability and avoids areas of air present inside the cast parts.

Chemische Analyse in Gew.%				
	C	Si		Fe
Ist	0,008	3,12		Basis
Min		2,70		Basis
Max	0,02	3,30		Basis

Andere: <0,2% (einzeln); <0,5% (gesamt)

Figure 4.2: Iron Silicon Alloy

4.4   Sample Types for printing characterization

Two types of samples were produced (see Fig 4.3):

- Cubes (DOE) to analyze the density and then characterize the machine parameters

- Toroidal-sized samples comply with the standards for magnetic measurements.
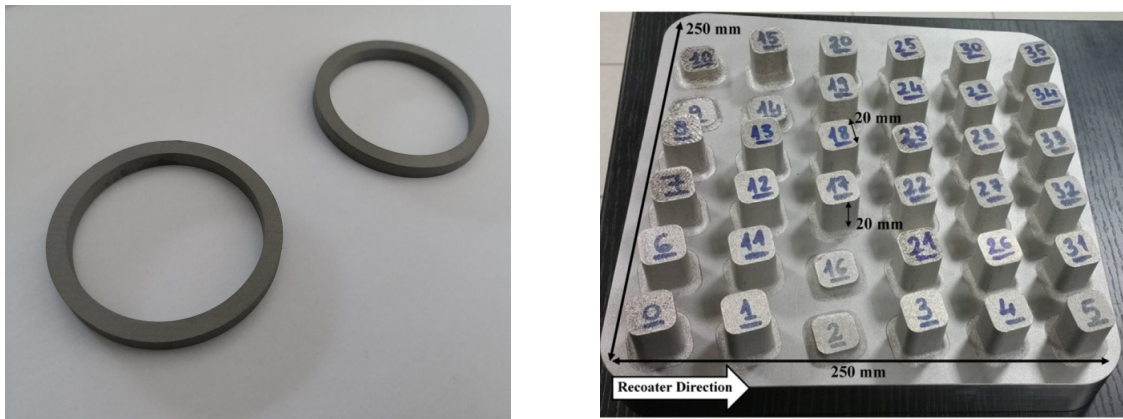
((a)) Ring samples

((b)) Cubes samples

Figure 4.3: Samples of FeSi3% produced by LPBF

To study the magnetic properties of the material and the influence of the machine parameters on it, a small toroid was printed along the Z direction of printing with the following dimensions: outer diameter 13.35 mm, inner diameter 9.58 mm, and thickness 2.25 mm The printed samples were made by anchoring them to the printing platform employing support structures to facilitate their removal and decrease warping.

Figure 4.4: Little Ring samples

4.5 System Settings for Silicon Iron Processing

The optimal machine parameters for printing this material were chosen through the realization of the DOE and subsequent study on the density of these cubes. From an electrical and magnetic point of view, the best performances are obtained for low porosity and crack values because in the presence of these factors the magnetic domain move with difficulty. Therefore, several samples were produced by keeping parameters such as laser beam focus position, hatch-spacing, scan distance, and layer thickness fixed and by varying others such as laser power (P) and scan speed (v). As for the scanning strategy, at each layer, the scan rotated by 67 °. The parameters chosen by this study for printing the toroids are shown in Tab.1:

PARAMETER	LEVEL
POWER, P, (W)	200
SCAN SPEED, V, (mm/s)	800
HATCH DISTANCE, HD, (µm)	70
LAYER THICKNESS, Z, (µm)	30

4.6 Heat-treatment of the Manufactured Parts

To study the effect of the annealing temperature on the microstructural evolution and on the magnetic and electric properties of the samples, the cubic and the ring samples were annealed at four different temperatures 400°C, 700°C, 900°C, 1200°C. The micrographs in figure 4.5 show the grain structure of the samples in

the as-built condition and after heat treatment at 1200°C in vacuum 1h. It is possible to see how the heat treatment stretches the grains, making the microstructure more homogeneous, but not the size of the grains, even if they are prominent. In particular, while the largest grains are predominantly equiaxed, much smaller grains are also visible, suggesting the incomplete recrystallization process. As re-

((a)) As-Built

((b)) As-Built

((c)) Annealed

((d)) Annealed
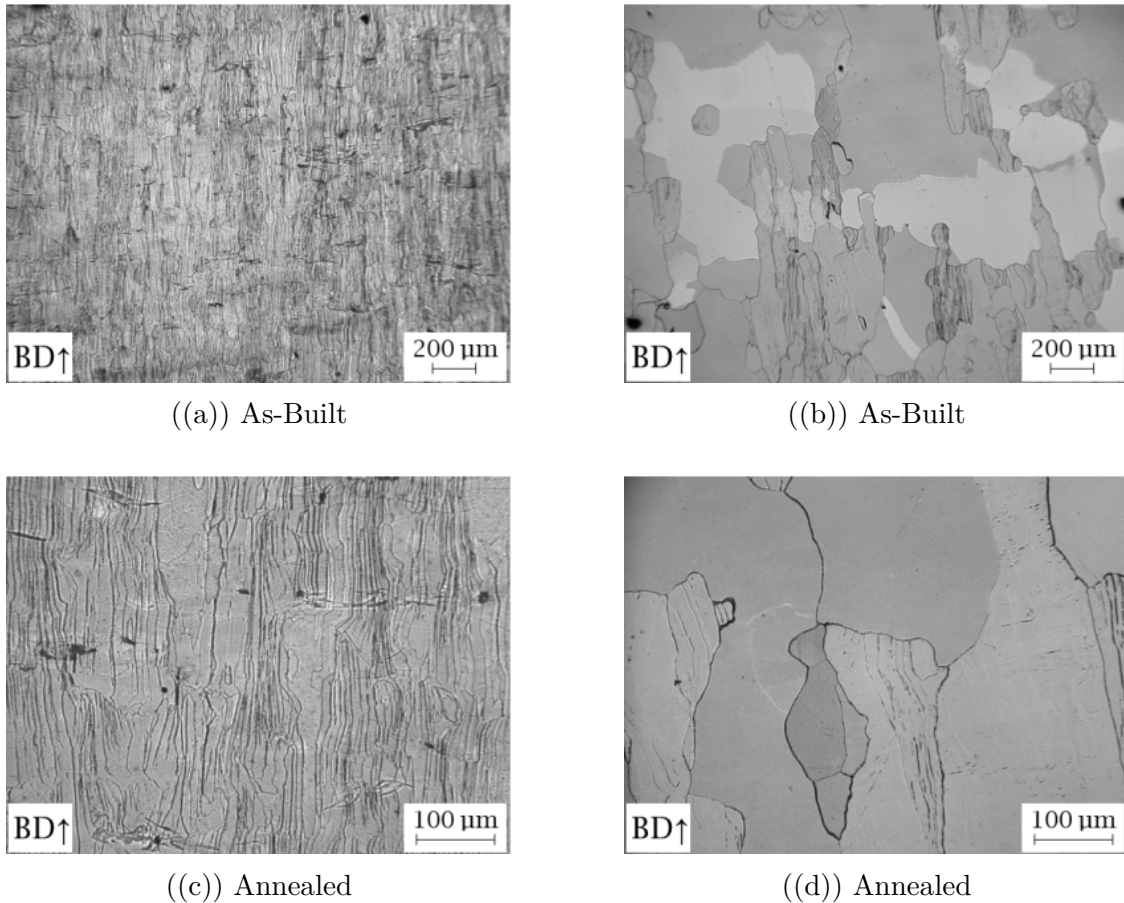
Figure 4.5: The average and standard deviation of critical parameters: Region R4

ported by Garibaldi et al.[72], the annealing does not significantly alter the <001> texture induced by LPBF along the Building Direction (BD). This phenomenon is positive as it allows to apply of heat treatment at high temperatures without compromising the crystallographic texture induced by the LPBF construction. In conclusion, the LPBF technique has the potential to manufacture grain-oriented iron silicon steels for magnetic applications. The <001> directions are the "easy axes" of magnetization, and the grain size after annealing is desirable for magnetic applications.

4.7   Characterisation of the Magnetic Properties

The material's magnetic properties were evaluated following the IEC 60404 series standards for the AC and DC measurement of the magnetic properties of soft magnetic materials using ring samples. The measurements were carried out on the as-built toroids and those after the various heat treatments illustrated in the previous paragraph. These measurements were done to evaluate the influence of annealing on the material's magnetic properties. In addition to evaluate the hysteresis cycle through a coercimeter, it was possible to evaluate the variation of the value of the coercive field as a function of the heat treatment.

4.7.1   Measurement of the Magnetic Properties

The apparatus used to evaluate the magnetic properties is illustrated in figure 4.6. A power amplifier increase the signal produced by a DC and AC voltage generator with the current i1 = v1 / R1, where V1 is the voltage given by the voltmeter connected to a shunt resistor R1. The measuring system is controlled through a LabView application. The magnetic field H is then evaluated using the formula H = N1 * I1 / l, where l is the average magnetic path length. The induced magnetic field B produces a voltage on the terminals of the secondary connection of the windings. The induced voltage is then integrated by a fluxmeter whose output is sent to the LabView application. This output voltage is evaluated as B = kV2 / AN2 + B0, where k is a calibration constant of the fluxmeter and B0 is the initial magnetization value. In the case in question, before the test, the samples were demagnetized for which the initial value of B0 was zero. The repeatability of the measurements was confirmed by carrying out three measurements for each sample. Considering the AC measurements, the parameters of interest are the specific losses in the material and the magnetic flux density. The tests were conducted at different frequencies, between 10 Hz and 1 kHz. The measurements were limited to an excitation field peak of 6500 A/m or a secondary voltage peak of 10 V. The toroidal sample was equipped with two windings: the secondary one, thinner, directly on the sample surface, and the primary one on top of the former. The Comparison between the measurements conducted before and after the heat treatment shows different properties of the material. The main differences involve the maximum magnetic permeability and the total iron losses. The magnetic permeability before the heat treatment is lower than expected for the adopted powder composition,
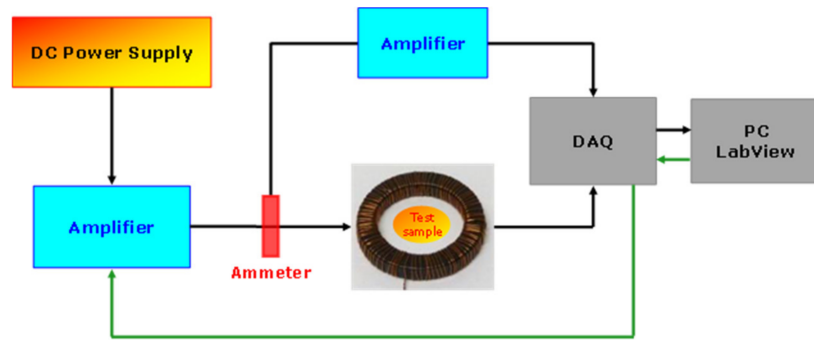
Figure 4.6: Experimental setup used to perform magnetic measurement on toroids samples (Reported from: Effect of the Temperature on the Magnetic and Energetic Properties of Soft Magnetic Composite Materials)[73].

mainly showing a poorly relaxed state of the crystal lattices. Consequently, the magnetization curves are too narrow and smooth. The maximum magnetic permeability value is 748 and magnetic induction. The results obtained are reported in figure 4.7 and 4.8 The magnetic permeability rises consistently after the heat treatment (Fig. 4.8(b)), bringing the hysteresis contribution to the iron losses to very low levels. The maximum magnetic permeability after the heat treatment corresponding to 3224 and magnetic induction show values greater than 1.2 T (Fig. 4.7(a)). The total iron losses after the heat treatment surprisingly decreased at all frequencies and for any peak induction value, as reported in Fig. 4.9(a) and Fig. 4.9(b). So the heat treatment benefits fully compensate for the reduction in global electrical resistivity. The hysteresis cycles before the treatment are reported in Fig. 4.10(a); it is possible to note the high presence of hysteresis losses and the contribution of eddy currents. The complete cycles at 1 T show a strongly reduced electrical resistivity, typical of a fully sintered internal structure (Fig. 4.10(b)), in which the central part of the iron losses is dynamic and originates from the eddy currents. The particular additional investigation concerns the maximum magnetic permeability as the function of the frequency, as shown in Fig. 4.11(a). The reduction is more pronounced after the heat treatment, and at 100 Hz, the reached value is 50% compared to the maximum one. A similar percentage decrease is obtained at 400 Hz for no heat treatment. The iron losses @1T for various frequencies are shown in Fig. 4.11(b). The values for with and without heat treatment are very close, whereas the values corresponding to heat treatment are minor.

47
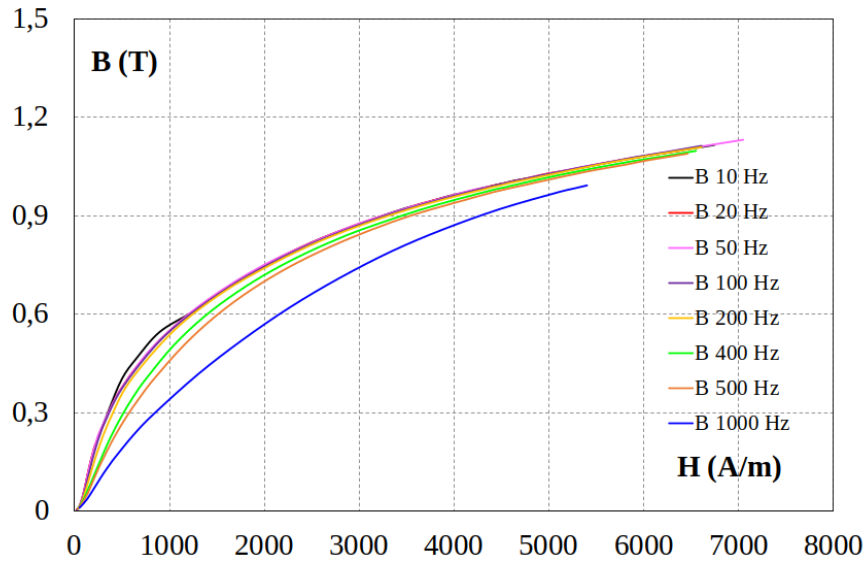
((a)) Magnetization curves at different frequencies for FeSi2.9 toroid without treatment
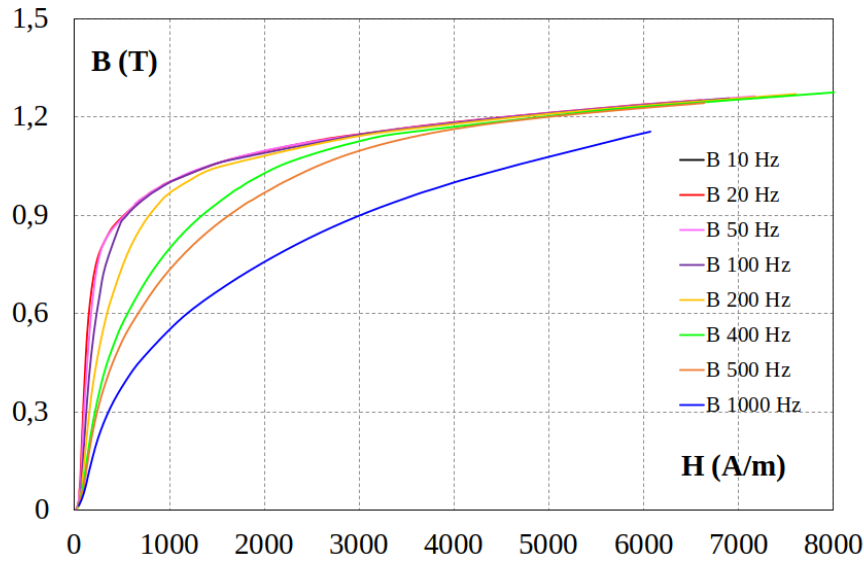
((b)) Magnetization curves at different frequencies for FeSi2.9 toroid with the treatment at 1200°C

Figure 4.7: Results of magnetic ring test analysis: Magnetization curves at different frequencies for FeSi2.9 toroid
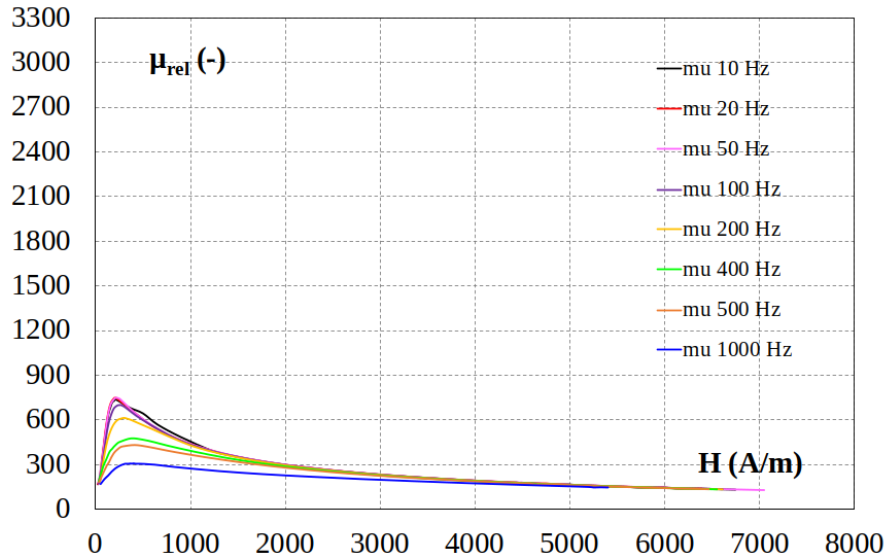
((a)) Magnetic permeability as a function of magnetic field H at different frequencies for FeSi2.9 toroid without treatment
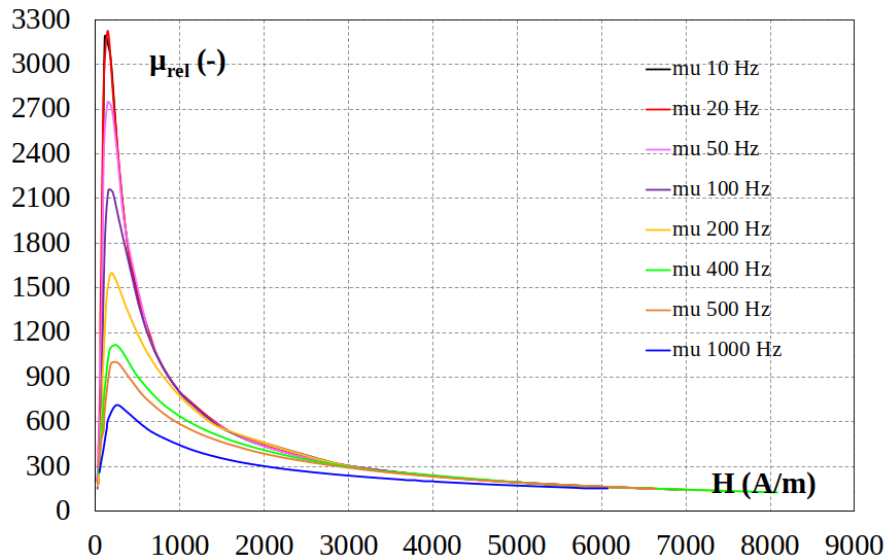
((b)) Magnetic permeability as a function of magnetic field H at different frequencies for FeSi2.9 toroid with the treatment at 1200°C

Figure 4.8: Results of magnetic ring test analysis: Magnetic permeability as a function of magnetic field H at different frequencies for FeSi2.9 toroid
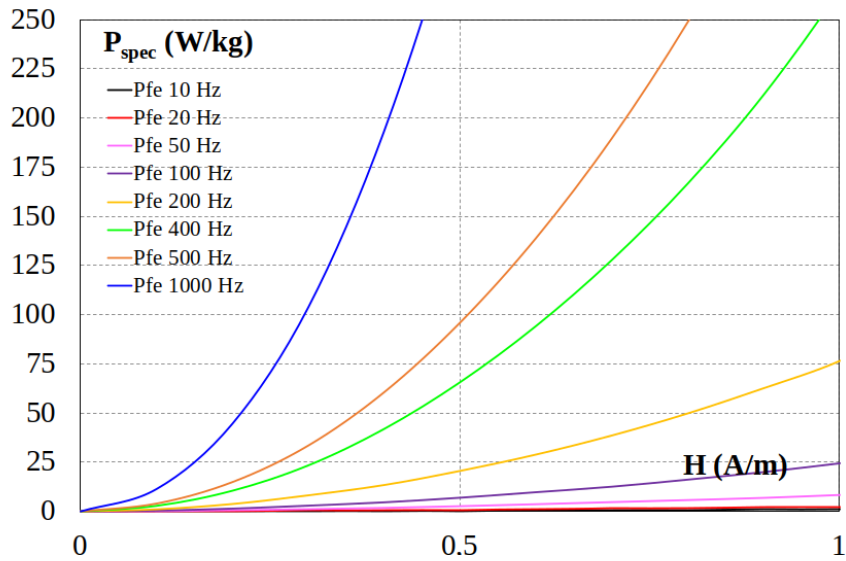
((a)) Specific iron losses as a function of magnetic induction at different frequencies for FeSi2.9 toroid without treatment
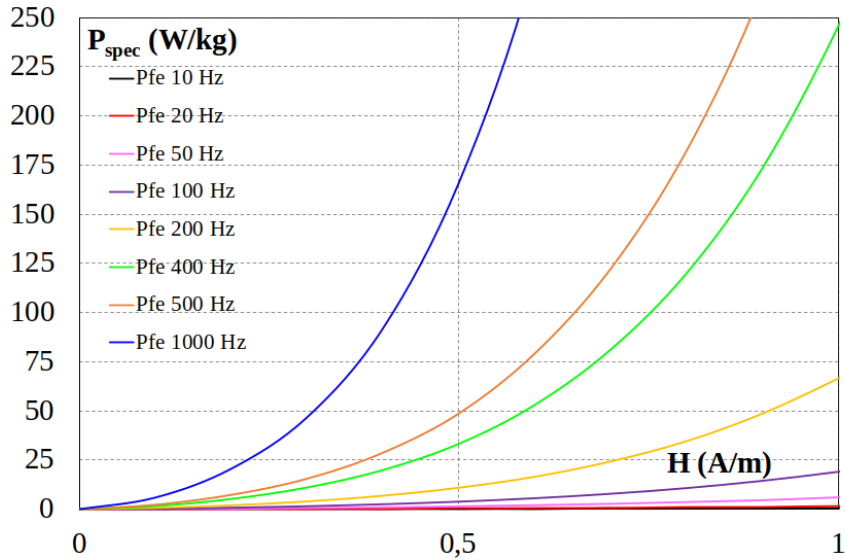
((b)) Specific iron losses as a function of magnetic induction at different frequencies for FeSi2.9 toroid with the treatment at 1200°C: restricted to 250 W/kg

Figure 4.9: Specific iron losses as a function of magnetic induction at different frequencies for FeSi2.9 toroid
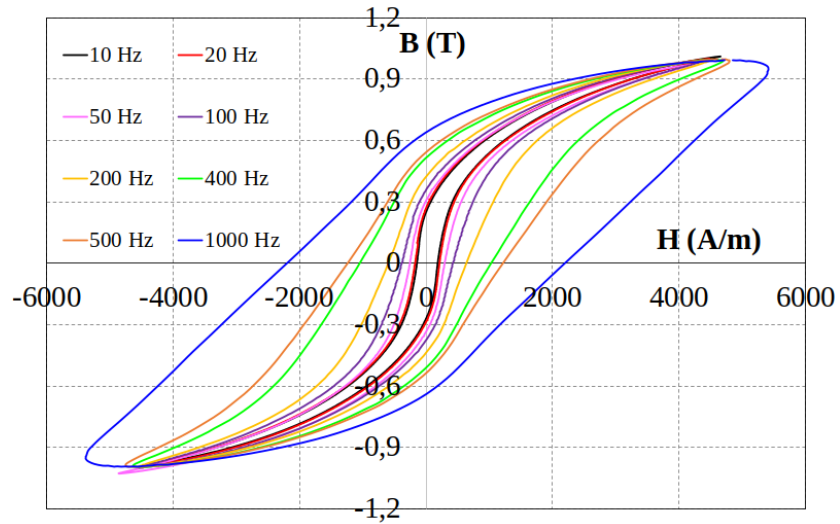
((a)) Hysteresis cycles at different frequencies for FeSi2.9 toroid without treatment
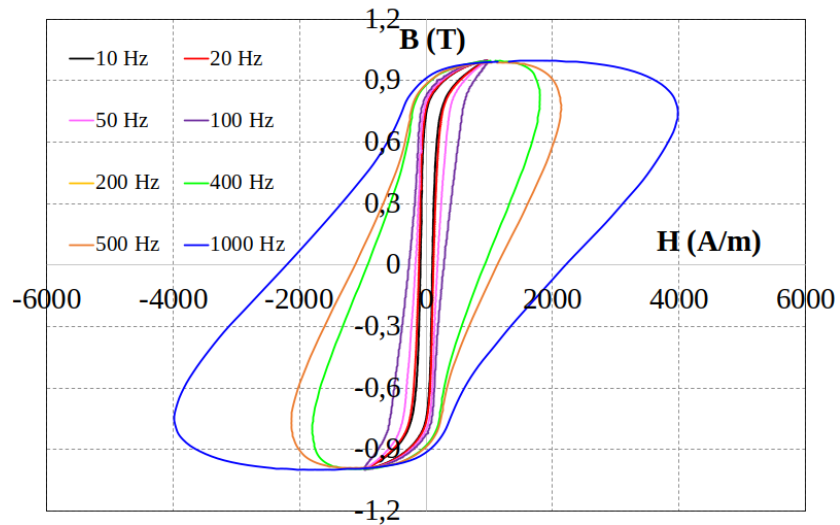
((b)) Hysteresis cycles at different frequencies for FeSi2.9 toroid with the treatment at 1200°C

Figure 4.10: Hysteresis cycles at different frequencies for FeSi2.9 toroid
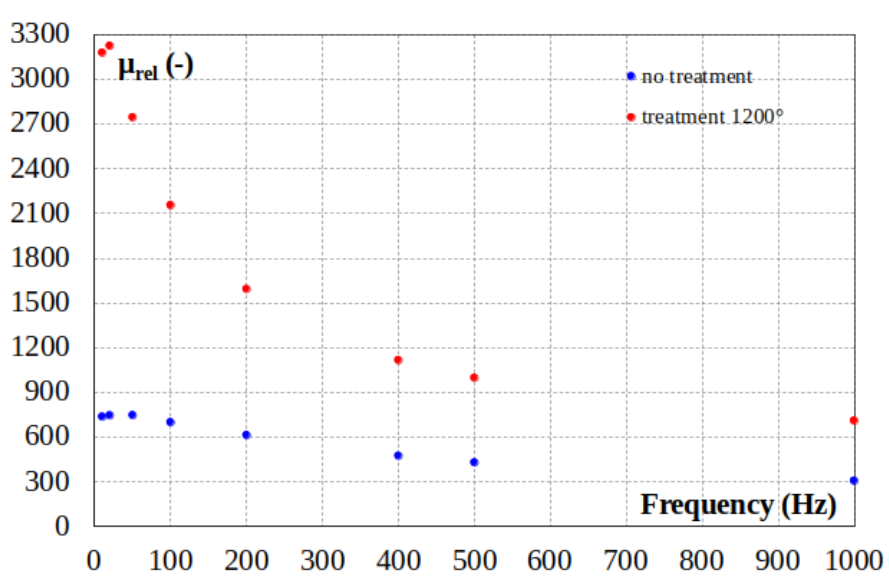
((a)) Comparison between magnetic permeability before and after thermal treatment as a function of frequency
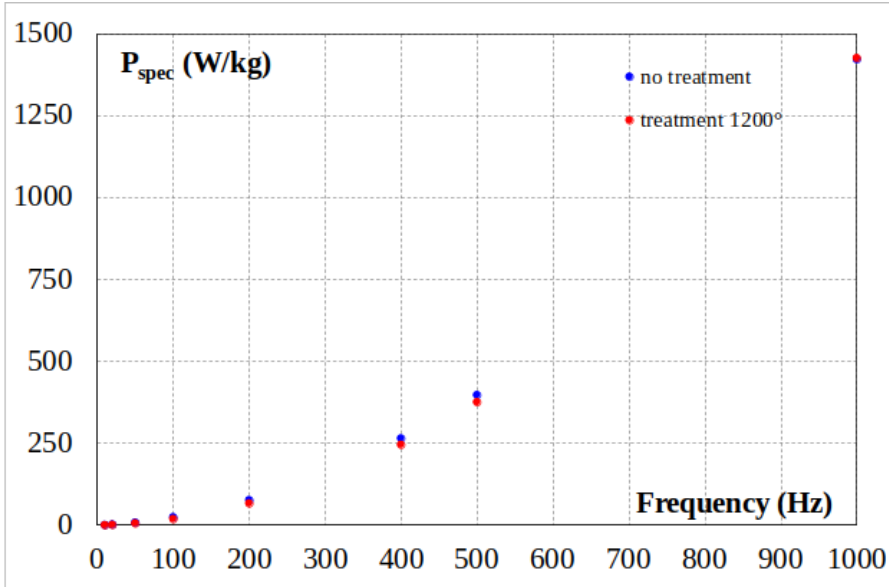
((b)) Comparison between specific iron losses before and after thermal treatment as a function of frequency

Figure 4.11: Comparison between magnetic properties before and after annealing

4.7.2 Coercivity Measurement

The coercivity value (Hc) measured in a very slow transient is highly related to the area of the hysteresis cycle. A controlled power supply, an excitation coil, and two sensing coils are the main parts of the adopted coercimeter (Fig. 4.12). The maximum magnetic field value reached in the saturation phase is 100 kA/m, while the Hc point is reached in 10 seconds, limiting most of the eddy current contribution. In Table 2, the results established the expected material behavior: an important depletion is evident in the residual stresses due to the fast cooling cycles induced in the LPBF process, as can be seen by the strongly reduced values of the thin and thick bars. This efforts should be better investigated in the future, as it can be related to the specimen shape or the printing conditions of such a small shape.

Figure 4.12: Coercimeter measurement
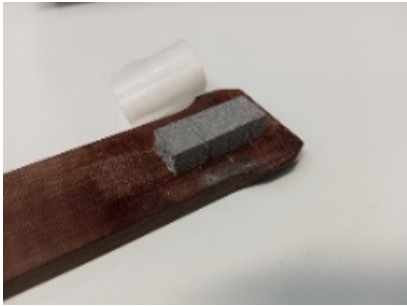
Specimen Shape	No treatment (A/m)	Treatment at 1200°C in vacuum (A/m)
	212	85.6
	151.6	94.6

Table 4.1: Coercitivity measurements of FeSi2.9 samples

Chapter 5

Electrical Application

After the studies conducted on the magnetic characterization of the printed material, the possible applications were considered. There are many cases in which the realization of the rotor for electrical machines, or transformers, was considered like application. In this chapter, the cases found in the literature will be briefly described, and new applications will be presented that, up to now, have not been considered(Electromagnetic device, Electromagnetic shield)

5.1 Electromagnetic device

One of the produced FeSi2.9 samples is the cursor for a small magnetic piston. This device is based on a coil, magnetically pulling a solid inner cursor. The used model is of the single effect type, thus including a counteracting spring. The nominal voltage of the device is 12 Vdc. After the LPBF process, the sample needed to be machined to obtain smooth surfaces and the thread for the end damper and nut, because due to their small size it was not possible to include them in the print(Fig. 5.1).

The tests on the device with the original and the newly produced rods, shown in Fig. 5.2, led to a direct electrical and mechanical comparison between the materials.

During the tests, a voltage step at the nominal level (12Vcd) caused the cursor movement until the natural stop position (Fig. 5.3).

The recorded voltage and current waveforms are shown in the figures (Fig. 5.4(a),Fig. 5.4(b), and Fig. 5.4(c)). Due to the low force on the FeSi cursor, the spring was not included in the setup. The initial cursor position was moved from
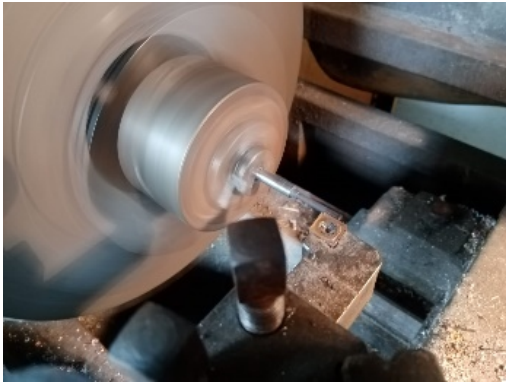
((a)) Removal of front roughness

((b)) Removal of side roughness

Figure 5.1: Machining of the sample

((a))
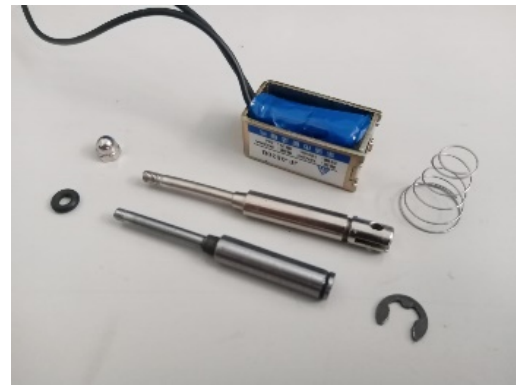
((b))

Figure 5.2: The original and FeSi2.9 plunger (a) and solenoid closing system (b)

the completely open one to an intermediate level so that the total stroke was, 10 mm. In the first transient test, the coil had no cursor inside, so only the electrical contribution to the current transient is visible (Fig. 5.4(a)). The presence of the cursor in the second and third tests changed the current waveform, showing the cursor travel phase and the time at which the movement was completed. The latter can be easily detected as the last current slope inversion, after which the current complete the exponential transient following the higher final inductance value. The main result is to show that the lower force acting on the FeSi rod causes a reduced acceleration (Fig. 5.4(c)), with a longer travel time, concerning the original rod (Fig. 5.4(b)). Future improvements to the test bench could lead to the measurement of the transient speed trend or the force acting on the cursor at different positions.
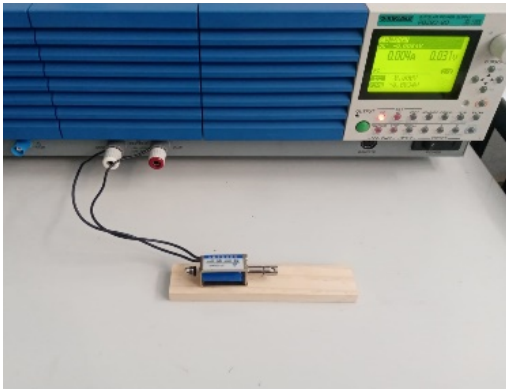
((a))
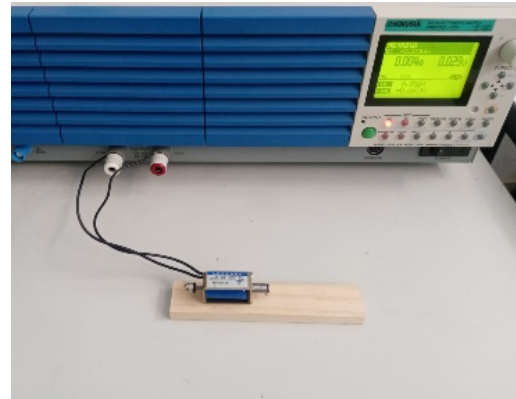
((b))

Figure 5.3: Plunger closing measurements: original (a) and FeSi2.9 (b)
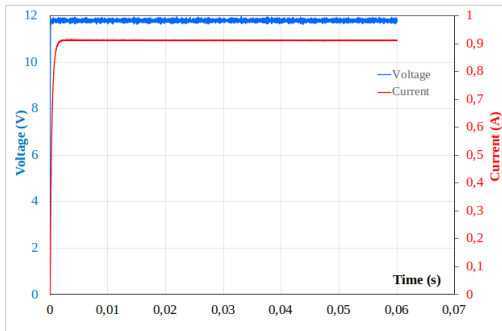
((a)) Initial current transient: Solenoid only
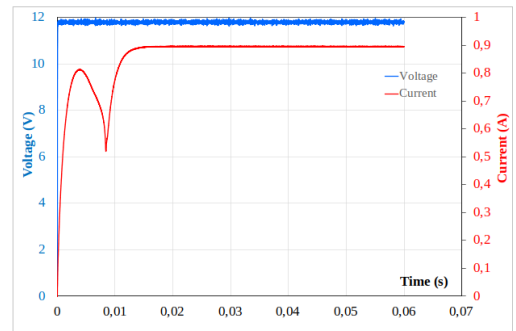
((b)) Initial current transient: Original small plunger
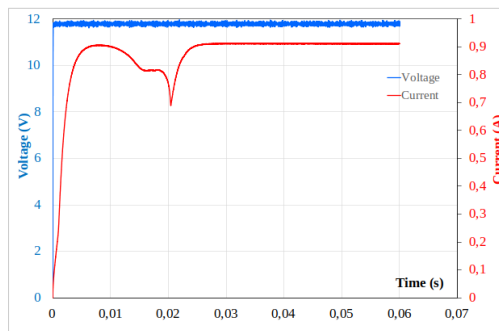
((c)) Initial current transient: FeSi2.9 small plunger

Figure 5.4: Initial current transient

57

5.2 Electromagnetic shield

5.2.1 Magnetic Shielding Theory

Most electromagnetic shielding is made from conductive or ferromagnetic materials. It should be noted that in the case of ferromagnetic materials, the permeability µ decreases with frequency. Presently, low frequency magnetic field shielding is a topic of interest for various applications, ranging from mitigating power line sources to protecting sensitive instrumentation. At low frequencies, the magnetic field is due to the electric current flowing in conductors of various geometries or to the magnetization of nearby ferromagnetic materials. The usual strategy to reduce quasi-static magnetic fields is to insert a shield of appropriate material whose properties are used to alter the spatial distribution of the magnetic field. The shield causes a change in the pattern of the field, deflecting the lines of magnetic induction away from the shielded region. A measure of the effectiveness of a shield in reducing the magnitude of the magnetic field at a given point is the shielding effectiveness SE, defined as: SE=|B 0(x,y,z)|/|BS (x,y,z)| Where B0 is the magnetic induction at a certain point when the shield is absent, and BS is the equivalent with the shield applied. When the shield is applied, the magnetic flux lines generally depend on the geometry of the shield, the material parameters, and the frequency. In addition, shield thickness is also another key factor; if working at a frequency such that the magnetic field is penetrating, a thicker shield leads to better shielding. The physical mechanisms that come into play when shielding low-frequency magnetic fields are flux shunting and eddy current cancellation. Ampere's and Gauss' laws determine the mechanism of flux shunting. To satisfy both conditions simultaneously, the magnetic field and magnetic induction can change direction when crossing the interface between two different media. At the interface between air and a ferromagnetic shielding material with a large relative permeability, the field and induction on the air side of the interface are pulled toward the ferromagnetic material almost perpendicular to the surface. In contrast, on the ferromagnetic side of the interface, they are led along the shield almost tangentially to the surface. The overall effect of the shielding structure is that the magnetic induction produced by a source is deflected into the shield, then deflected within the material in a direction almost parallel to its surface, and finally released back into the air. Due to a time-varying incident magnetic field, the current cancellation mechanism is determined by the

eddy currents formed in the shield material. As described by Faraday's law, when the shield is exposed to a time-varying magnetic field, an electric field is induced within the material. When the shield is highly conductive, an induced electric current density is driven as described by Ohm's law. The induced current density gives rise to a magnetic field opposite the incident field, which is then repelled by the metal and forced to run parallel to the shield's surface, producing a small magnetic induction within the metal.

5.2.2 Case study

A shield with ferromagnetic material (FeSi2.9) was produced using the LPBF technique taking as a geometric reference an actual conductive shield of a relè. The chosen growth direction of the shield on the print bed is that in the x-y plane. The system was characterized using two different sources of magnetic field excitation DC and AC / DC, considering two different orientations, Z and Y, as described in Fig.5.5
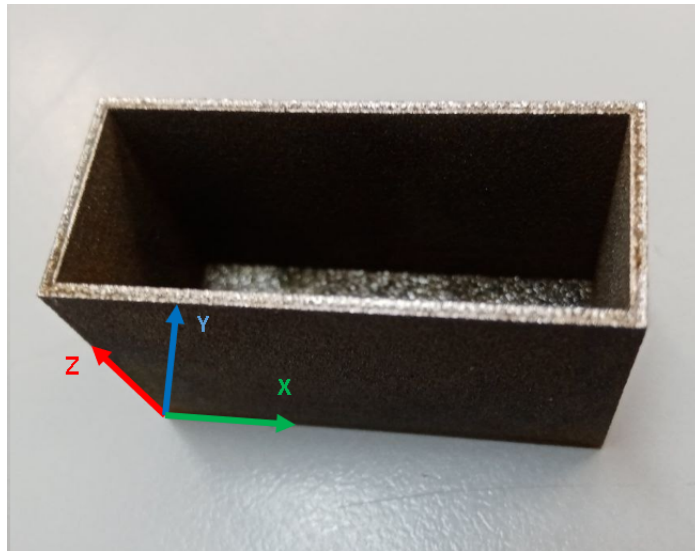
Figure 5.5: FeSi2.9 Shield

Measuring apparatus

The measurements were made considering two different directions of the magnetic field. Along the Z and Y axis. In Fig. 5.6, the structure used for the

measurements is shown. The reported results are calculated using three configura-
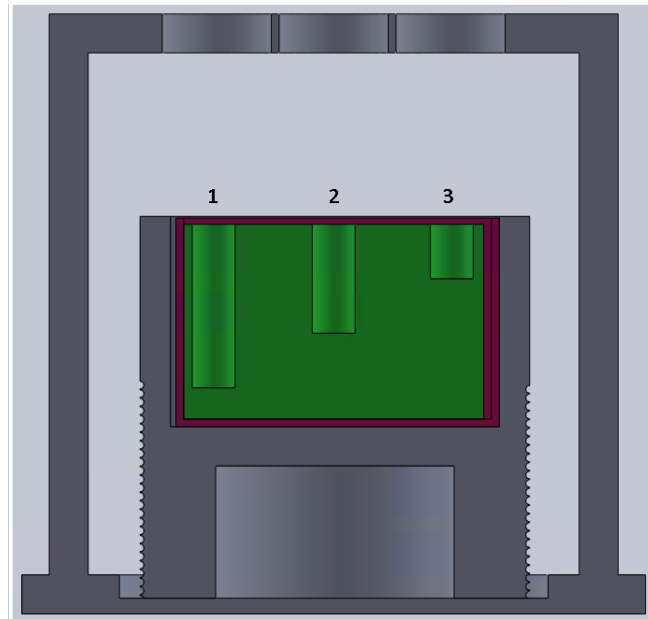
Figure 5.6: Measuring Apparatus

tions: traditionally manufactured aluminum shield, additively manufactured ferro-
magnetic shield, and additive manufactured ferromagnetic shield after annealing at
1200 ° C for 1h in vacuum. To evaluate the shielding performance of these objects,
a parallelepiped in PLA was made using the FDM technique with three holes for
inserting the probe at different heights inside the shield, as shown in Fig.5.7.
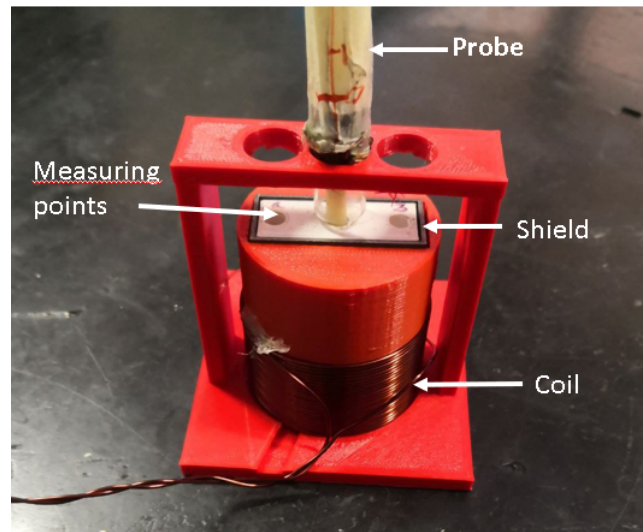
Figure 5.7: Probe Support Structure

DC Magnetic field excitation

Fig.5.8 shows the measurements made using a permanent magnet as a source of the DC magnetic field. What is noticed in both cases is the anisotropic characteristic of the material. The reason for this is that the growth direction of the workpiece in the printer coincides with the direction of easy magnetization of the material; this was demonstrated in [60]. So, the SE values are much higher in the axial direction than in the transverse direction. Although the properties of the part produced in AM are not performing than the aluminum shield (see orange and blue column, respectively), this cannot be said after heat treatment (grey). This type of heat treatment can increase the electrical and magnetic properties of the piece due to the microstructural change described in section II, thus favoring an increase in the shielding properties.
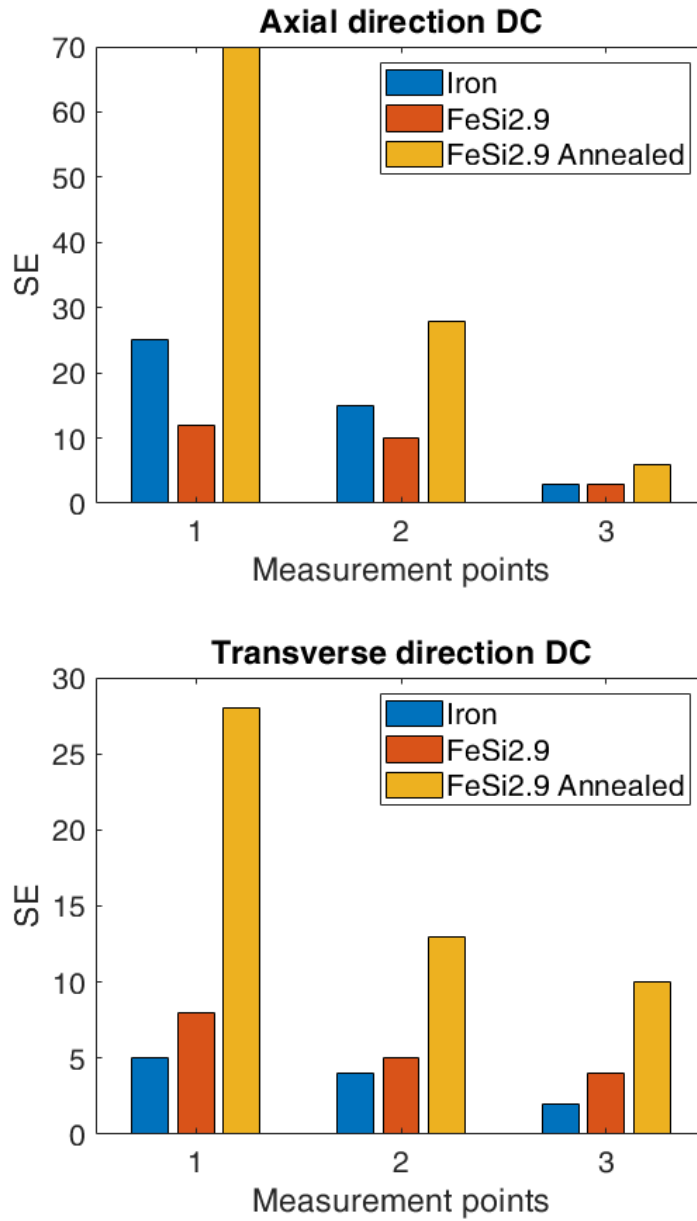
Figure 5.8: SE DC excitation Axial and Transverse dircetion

AC/DC Magnetic field excitation

With the alternating current power supply, phenomena described in paragraph 1 contribute to better shielding of the external field. Also, in this case, the heat treatment's improvement effects and the shield's anisotropic characteristics are noted in Fig.5.9 and Fig. 5.10.
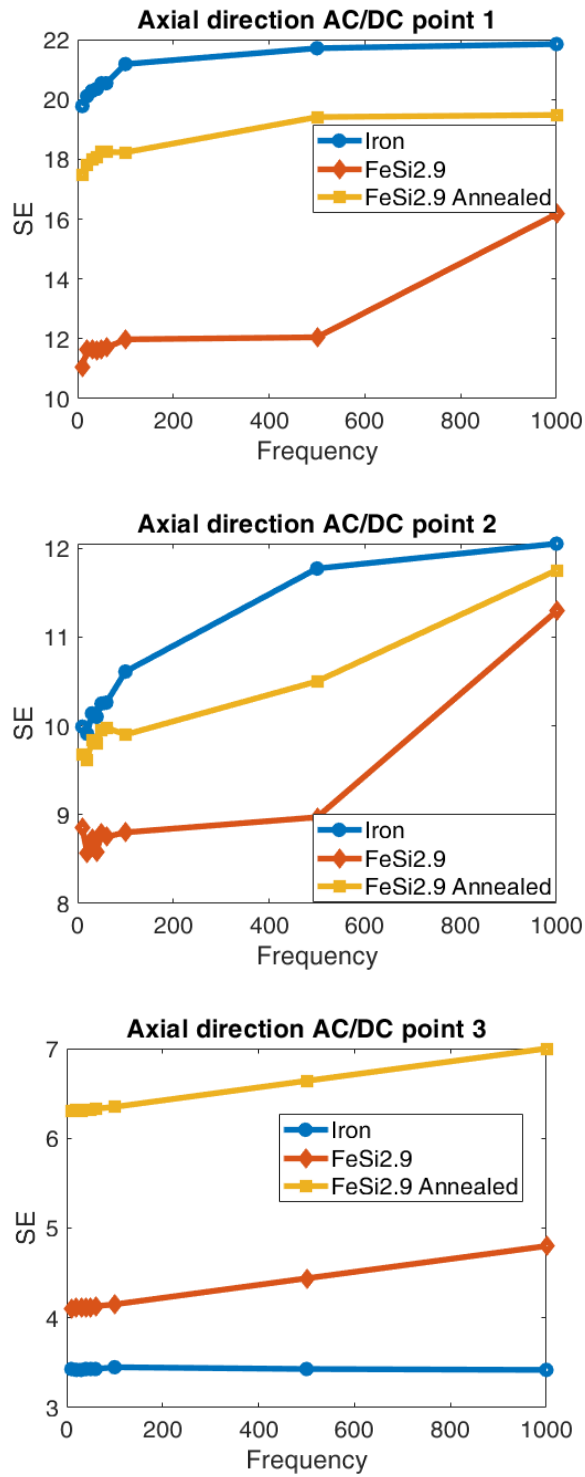
Figure 5.9: SE AC/DC excitation Axial direction

63
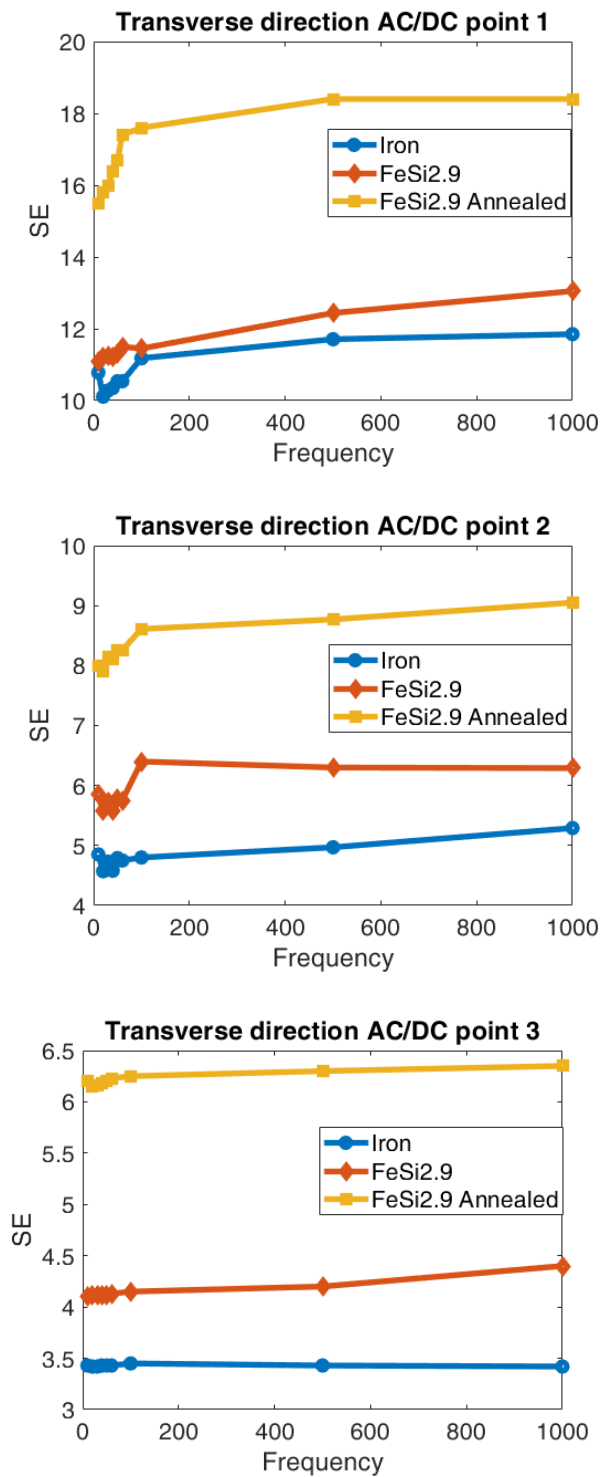
Figure 5.10: SE AC/DC excitation Transverse direction

5.3   Results

Comparing the graphs for the case in DC and the cases in AC / DC, it is possible to say that:

- In stationary conditions, for all measuring points, the ferromagnetic material in the as-built condition has a shielding factor comparable to the traditionally produced shield. On the other hand, after heat treatment, the value of SE increases enormously for measurement point 1, the deepest one and therefore closer to the screen, compared to the other two measurements for the axial and transversal case.

- The different values for the axial and transverse cases are due to the anisotropic characteristic of the printed component. This is a significant result to be taken into consideration for the correct design of future AM-produced shields

- For cases in alternating current, what has been said in the previous points is valid; moreover, additional considerations can be made. In particular, it is possible to notice the effect of eddy currents which, although considered losses, in the case of shielding, help to increase the shielding factor.

- For the case of axial measurement in AC / DC, referred to as measurement point 3; it is possible to notice a different trend compared to the previous points. This inversion is because point 3 is located near the edge of the screen. Therefore, in addition to the dissipative effects for eddy current, the effects at the edges increase the shielding factor at that point.

- Finally, taking into consideration the transversal cases carried out in AC / DC, we can conclude that in this direction, the eddy current losses are higher than the axial cases; therefore, both in the as-built and annealed conditions, there is a more significant shielding factor. This feature is due to a different microstructure between the base of the shield and the walls of the same.

5.4 Conductive Material

With the recent technological implications, enormous scientific interest has been shown in manufacturing copper components for electrical applications. Several copper alloys are available on the market with different conductive and mechanical properties. Pure Copper, interesting for its electrical and thermal conductivity properties, can be printed with a density close to 100% if a green laser is used as a powder melting source. Among the recent applications that are best suited both for the use of technology and for the properties deriving from the printing of this material, we find heat exchangers and inductors for inductive heating, stator, or rotor windings. The figure 5.12 shows some application examples. On this
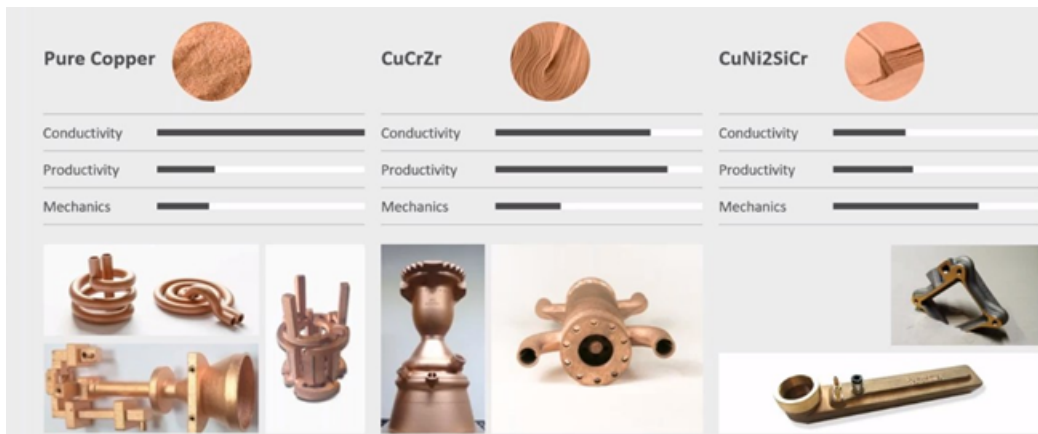
Figure 5.11: Example of applications of Copper(Reported from: eos.info)

front, the printed material was also characterized to verify its electrical properties. The copper alloy used is CuNi2SiCr. Different samples were made for different characterizations, as reported in the figure. The results show that this copper alloy is more suitable for mechanical and thermal than electrical applications. The tests concerned the measurement of the material's resistivity on a bar of the same material by means of a four-wire test using a system consisting of the following two PC-controlled instruments: Fluke 5720A multi function calibrator - sn 7415202, working as a direct current generator and Keythley 2002 digital multimeter - sn 0640745, used as a direct voltage meter. The program makes successive polarity changes on the current, in order to allow the elimination of offsets due to the multimeter. The four-wire test is reported in fig 5.13, it consist by passing a current through two outer probes and measuring the voltage through the inner
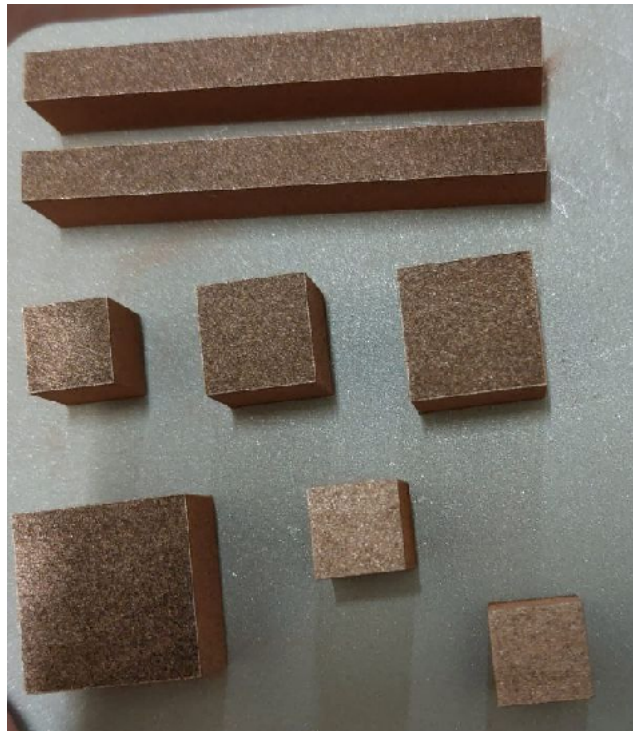
Figure 5.12: Example of Copper samples

probes. Using Ohm's second law (5.1), it was possible, knowing the geometry of the piece, to derive the resistivity of the material and so the electrical conductivity.
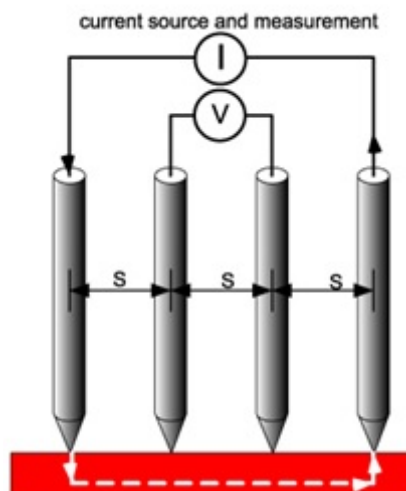
Figure 5.13: Four wire test (Reported from:https://www.pveducation.org/pvcdrom/characterisation/
point-probe-resistivity-measurements)

$$R = \rho \cdot \frac{l}{S} \tag{5.1}$$

The value of electrical resistivity measured for this copper alloy is equal to $4.77 \cdot 10^{-7} S/m$

Chapter 6

Non-destructive testing

The lack of robustness, stability, and repeatability of AM processes means that the presence of defects is still too high compared to conventional production systems. The review article by Grasso e Colosimo [74] offers an overview of the different types of defects and their causes, which is useful to recall. In PBF processes, which include SLM and EBM technologies, they can be various types of defects were found due to different generation mechanisms:

- Porosity. It consists of voids (cavities) within the massive molten material. These gaps can be found in a layer, between adjacent layers, or on the outer surface of the part. Pores can be spherical or circular (those between the layers) and have a size of a few microns. Porosity has a strong impact on the growth rate of the cracks and, therefore, on the fatigue performance.

- Balling. It consists of forming fused spheres, which occurs when the molten material solidifies into spheres instead of in solid layers and constitutes a severe impediment to the connection between the layers. Surface tension guides the balling phenomenon, preventing the molten material from wetting the underlying layers. Balling can increase the surface roughness, as many pores can form between the metal spheres, while the spheres protruding from the layer of dust can interfere with the movement of the powder deposition system.

- Residual stresses, cracks, and delaminations. These defects are due to the onset of thermal gradients and the cooling phase of the melted layers. Delaminations are particular types of cracks that arise and occur to propagate

between adjacent layers.

- Geometric defects and dimensional accuracy. They consist of geometric and dimensional deviations (shrinkage, dilation, and distortion) from the nominal model. Various types of distortions (curvature, raised edges) deteriorate the surface topology and the part's dimensional accuracy. Such defects can worsen the stepped profile due to the layer-by-layer production of curved and inclined surfaces (stair-stepping effect). When the elevated vertices protrude from the dust bed, they can interfere with the covering system. Other types of critical distortions are the formation of thin walls and surfaces protruding and acute angles. In such regions, the molten pool is surrounded by dissolved dust, which has conductivity lower than the solid material. The lower thermal flow causes a local overheating phenomenon which can deteriorate the geometric accuracy.

- Superficial defects. The surface roughness is due to two contributions, the stair stepping effect and the roughness of the surface of the metal constituting the substrate. The surface finish depends on the orientation of the surface relative to the growth direction and affects the fatigue strength of the part. The balling effect can also produce a defective surface, which hinders obtaining smooth surfaces.

- Inhomogeneity and microstructural impurities. PBF processes involve highly localized heat inputs during the short times of beam-material interaction, which significantly affect the part's microstructure. The microstructure obtained by PBF processes differs from that obtained through conventional processes. There is a relationship between the microstructural properties and the formation of micro-pores, cracks, and residual stresses. Inhomogeneities of the structure include impurity, differences in the size of the grains, and differences in the crystallographic texture. The impurity of the material is represented by inclusions, contamination from other materials, and the formation of surface oxides. The presence of unfused powders inside the pores or in the form of lumps is responsible for the premature rupture of the samples due to the reduction of the useful section.

Defects in metals produced for AM can be grouped into the following categories according to their origin and cause: defects induced by the equipment, the process,

the model, and the supply of the material.

- Defects induced by the equipment. Defects due to the instrumentation are mainly attributable to the beam deflection and scanning system, environmental control of the work chamber, collection e powder treatment and deposition system, and insufficient substrate thickness. These problems can lead to a lack of fusion and produce different defects, including porosity and poor geometric accuracy. Contamination by gaseous products or the energy reflected by the powder bed can affect the local energy distribution of the beam. Even small changes in the oxygen composition can cause significant changes in the molten pool and affect the stability of the process. The oxygen content in the chamber is critical for generating the balling phenomenon. Defects associated with distortions, deformations, delaminations, and cracks are affected by the thickness of the substrate and how heat from the process is dissipated through the substrate. Preheating the powder bed is essential for lowering thermal gradients and tensions. Incorrect dust deposition can create irregular layers of dust, which hurt the physical interaction between the laser beam and the material.

- Process-induced defects. Defects caused by errors in the process are associated with the interaction between the beam, the melted powder, and the previously melted material. The scan strategy affects the temperature distribution on the slice and the generation of porosity and voids and could lead to the onset of tension residuals. Improper strategies can result in the generation of overhead vertices and affect their microstructural properties. The thickness of the layer influences the residual stresses in part and the initiation of the balling phenomenon. Process parameters, scan strategy, pore morphology, and component performance also affect the density of the part. The laser power, the scanning speed, and the distance between the traces determine the energy density. There is a correlation between energy density and component density, which allows the identification of a window of process parameters corresponding to good density and quality of the part. Another source of defects is related to the expulsion of particles and liquid metal due to the interaction between the beam and the material. When splashes fall onto the dust bed, they can produce two types of defects: voids and discontinuities in the material.

71

- Model-induced defects. The errors induced by the design choices implemented in the model can be carried out in the design of supports and sacrificial elements and the part's orientation concerning the substrate and the reference system of the machine. The anisotropic behavior of the product final is strongly related to the construction direction of the part, which eventually influences its own physical and mechanical properties.

- Defects induced by the supply of material. The quality of the powder is directly related to the process production. Flowability and bulk density have the greatest impact on product quality. Particles spherical and smooth enhance these two properties of the powder. Metal powders can be contaminated by moisture, organic compounds, adsorbed gases, oxide films, and nitrites on the surfaces of particles. Such contaminations can degrade the consolidated component's mechanical properties and geometric accuracy.

6.1 Experimental methodologies for evaluating the quality of products. Non-destructive controls

The use of AM processes has great potential for manufacturing high-value, complex parts customized and could revolutionize the production of parts in frontier sectors like that electrical, allowing the introduction of products with "design constraints" such that they cannot be manufactured using conventional processes, reducing waste (green manufacturing), eliminating the dependence on original equipment manufacturers (OEMs) for spare parts and extending the life of components in service through methodologies of innovative repairs [75],[76]. However, industry adoption of AM-made parts is slow due to the ambiguity in current validation and verification approaches, which are intimately related to the ability of the NDT. Existing non-destructive investigation methods and techniques are not, in general, optimized for processes, materials, or AM parts [77]. Furthermore, the application of ND in situ investigation techniques during the AM process is relatively new and needs further research. Conventional ND techniques for post-treatment checks of parts finished made by AM are demanding and have not yet been definitively finalized, date the variety of technologies and materials used in AM. Currently, the most used methods are:

- Ultrasound: The ultrasound technique (UT) allows the analysis of metallic and ceramics made using additive manufacturing processes to detect any defects and contribute to the validation of the processes developed and the qualification of the parts produced. Although ultrasonic testing is counted among the NDT techniques suitable for metal components made for AM [78],[79],[80], there are still few application examples in the literature. For example, in [80] the authors evaluate the ability to identify defects in materials made using processes of Welding Arc Additive Manufacturing (WAAM) by some NDT methods. Among the non-destructive techniques selected, there is also the UT one. The authors demonstrated that the UT method provides correct information on the location of defects, despite some limitations. The ultrasonic method is the most flexible regarding the positioning of the inspection instrumentation and can detect defects found in WAAM materials.

- Thermography: Thermographic methods detect surface and sub-surface defects. The thermographic approach used will be that active. Active thermography techniques are based on using an external stimulus (thermal or mechanical), which generates a response in the structure in terms of the evolution of the surface temperature, which is affected by the presence or absence of sub-superficial defects. Analyzing the maps of the thermograms acquired in the time, the defects generally reveal themselves in the form of thermal contrast.

- X-ray computed tomography: The AM process is certainly the most suitable for making parts with complex geometries, but these geometries pose a challenge to conventional CND methods such as ultrasound, eddy currents, and also radiography. Likewise, many parts made by AM have an internal structure that may not even be accessible to methods such as penetrating liquids and magnetoscopy, which are less sensitive to geometry. In addition, the irregular or rough surfaces in these parts make the traditional NDT methods for detecting surface defects, such as magnetoscopy, difficult or impossible to apply due to the high background noise due to the manufactured surface roughness. Added to this is the fact that finite AM parts typically have a major range of porosity and lack of fusion defects, with a distribution extended to the whole part, which renders difficult the a priori sizing of significant defects or the assumption of a single anomalous defect. Hence, the

most promising technique for complex geometric parts appears to be computerized tomography X-ray (CT). However, even CT has limitations. For example, the CT survey is unsuitable for linear defect detection and takes time for data acquisition and analysis (the visual interpretation slice by the slice is unavoidable). Furthermore, the sensitivity of the CT decreases when the parts become physically larger or thicker [81]. Current micro-CT systems may not have the penetrating power and resolution to detect critical defects in larger parts dimensions produced for AM. Despite the limitations mentioned above, the CT survey is the most suitable for investigating parts with complex geometry.

6.2 Evaluation of electrical conductivity of FeSi2.9 additive manufactured electromagnetic shield employing active thermography approach

6.3 Materials and method

The tests were carried out on electromagnetic shields of ferromagnetic material (FeSi2.9) produced using the laser powder bed fusion (LPBF) technique. In LPBF, a laser beam selectively melts the powder in a powder bed, generating a cross-sectional area. A component is built as several melting tracks are strung together in a micro-welding process. The experiment was performed on two samples: the as-built condition and annealed at 1200 ° C. In particular thermal diffusivity and mass were measured.

6.3.1 Active Thermography setup

The laser spot active thermography technique studies the thermal response of a component subjected to an external heat source, a laser beam. The experimental equipment was composed of a thermal camera, a laser excitation source, and a PC control unit. The IR thermal camera is a FLIR A6751sc with sensitivity lower than 20 mK and a 3-5 μm spectral range. At the same time, the laser source can generate a maximum power of 50 W concentrated on a small surface. The

experimental configuration was in "reflection mode," as shown in Figure 6.1. The initial experimental parameter are presented in table 6.1

Table 6.1: Initial parameters

Distance	Ambient Temperature	Relative humidity
53cm	26.6°C	39

For both specimens, the same test has been performed as presented in table 6.2

Table 6.2: Testing setup

Test	Technique	Step n°/ duration	Power level	Frame rate
1	PULSED	50ms	50%	329fps
2	PULSED	500ms	25%	30fps
3	LOCK-IN	15X50ms	50%	329fps
4	LOCK-IN	15X500ms	25%	30fps
5	LOCK-IN	15x2000ms	15%	30fps

The results of test 5 will be presented.

The lock-in test has been post-processed to obtain the phase plot of the thermogram.

The most common method to extract the signal phase is to use the fast Fourier transform. This is applied using the FFT command of Matlab software, analyzing the signal with this algorithm, and a 1D Fourier transform is applied to each pixel. The data are formatted as a tensor of three dimensions where the first two are the spacial dimensions (pixel), and the third dimension is the time dimension (frames).

A Fourier transforms analysis through the time dimension for each pixel to extrapolate his phase contribution. The result is a phase map plot of the phase value in each pixel as presented in figure 6.3

Plotting the value of the phase along an arbitrary axis passing through the center of the spot, the behavior is linear.

This is explained by analytical models, which correlate the thermal diffusivity to the phase slope with the distance from the laser spot.

It is visible an almost flat part which corresponds to the laser spot radius, while the linear part corresponds to the diffusion area of the heat during the lock-in pulsation. Because of the small dimension of the specimen and the long period

75
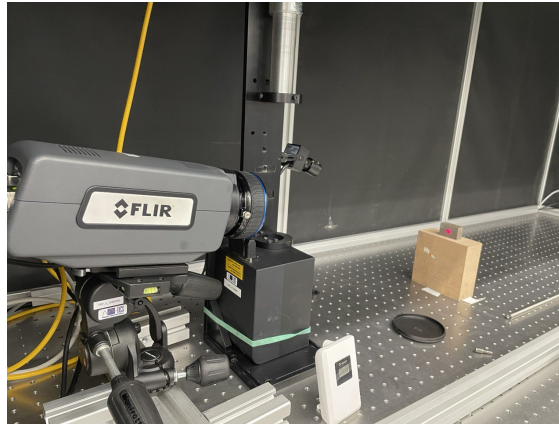
Figure 6.1: Test set-up
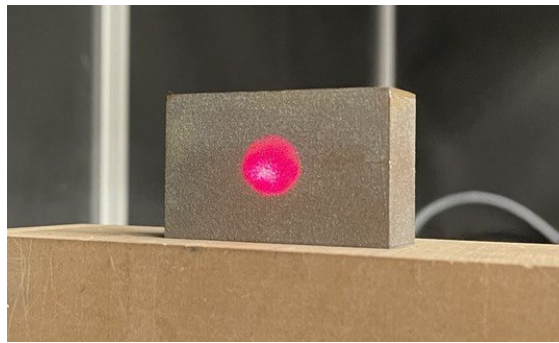
Figure 6.2: Particular of laser spot

of modulation of the laser, there are some nonlinearities due to boundary effects which make the lines not linear in the last part

The formula which correlates is

$$m = -\sqrt{\frac{\pi f}{D_x}} \tag{6.1}$$

Where m is the slope [rad/mm] of the curve, while f is the modulation frequency [Hz] of the laser spot lock-in technique and Dx is the thermal diffusivity along the x direction in which the phase/space diagram is done by cutting the phase map. The thermal diffusivity is defined as:

$$D_x = \frac{k}{\rho c} \tag{6.2}$$

A linear polynomial fitting is used to calculate m.
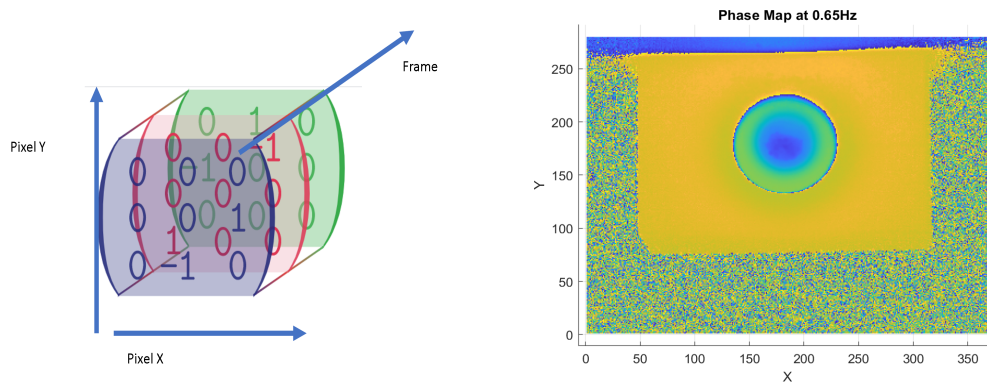
Figure 6.3: Signal tensor and phase map
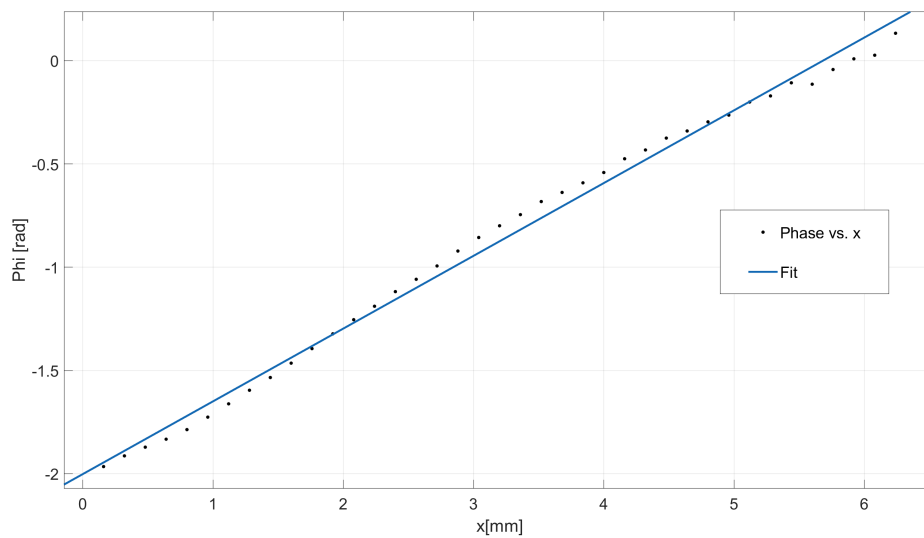
Figure 6.4: Fitting methodologhy

The modulation frequency is 0.5Hz (modulation period T= 2s)

Using eq.6.1, it is possible to obtain the thermal diffusivity along the studied direction. In this particular case, this methodology allows one to choose any direction without having boundary effects, even if the component has a small geometry.

6.3.2   Electrical conductivity measurement

6.3.3   Wiedemann Franz formulation

The Wiedemann and Franz correlation allows linking the thermal and electrical conductivity. It is an empirical formulation EQ.6.3 that it is possible to obtain the electrical property through the calculation of the thermal diffusivity. The advantage consists in being able to calculate the value of electrical and thermal conductivity on complex geometries without the need to make *ad hoc* specimens.

$$L = \frac{K}{\sigma T} \tag{6.3}$$

Where:

- L : 2.44 3 *10e-8

- T: Temperature

- K: Thermal conductivity

- σ : Electrical conductivity

6.4   Results

The thermal responses of the tested specimen are presented. The concept at the basis of this analysis is that a variation in thermal properties of the material can be measured as a phase delay of the thermal diffusion through the bulk of the material. The signal post-processing has been performed as presented in the Materials and methods section. From the phase diagram in figure 6.5, it can be immediately recognized that there is a different trend in the phase slope. The phase plot presented in figure 6.5 can be divided in three zones:1,2,3. Zone 2 corresponds to the laser beam heated zone. The laser produces a gaussian heat pulse which crates a plateau on the phase diagram. The dimension of this plateau is correlated to the laser beam radius. Zones 1-3 correspond to the specimen zones around the laser spot where thermal diffusion occurs. The idea is that the heat treatment of the additive manufactured specimen produces a decrease in the number of voids and an increase in thermal diffusivity.
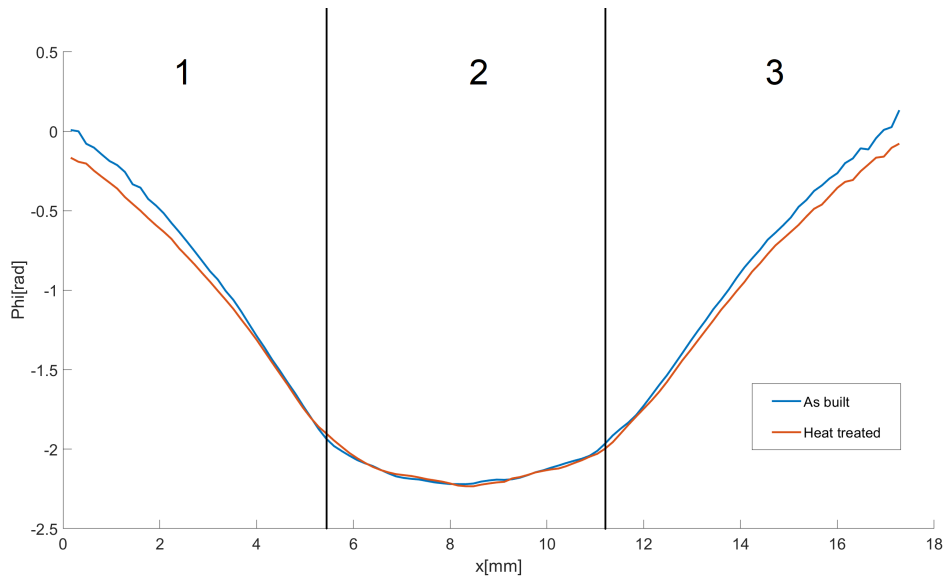
Figure 6.5: Phase cut

In figure 6.6, a particular phase diagram shows the difference in slope between the as-built and annealed specimen. These data were used for calculating slope parameters using polynomial fitting. What can be noticed is that after the annealing treatment, the slope of the curve is less steep. This means that the annealing increases the thermal diffusivity of the material.
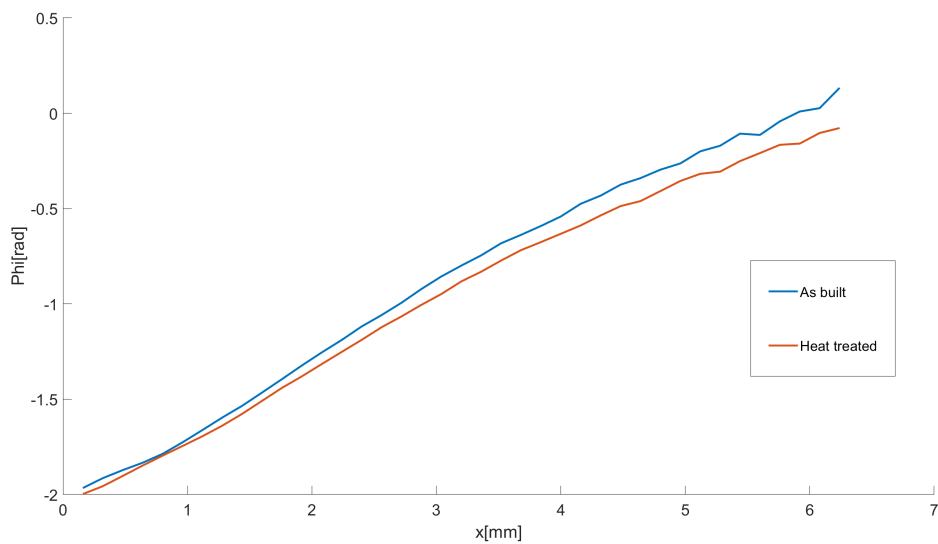
Figure 6.6: Phase slope

All the results obtained from the thermal measurement are therefore presented:

	As-built	heat treated
m[rad/mm]	0.3523	0.3302
D[mm2/s]	12.7	14.4
pore percentage	0.533	0.487
k[W/m2 K]	18.5	23

Table 6.3: Experimental thermal parameter

Using the Weidemann Franz law, the thermal conductivity obtained using the phase method can predict the electrical conductivity. The results of the experimental measurement of electrical conductivity and the predicted one are presented here:

	As-built	Annealed
$\sigma_{experimental}[MS/m]$	1.76	2.12
$\sigma_{predicted}[MS/m]$	1.80	2.24

Table 6.4: Conductivity values in the experimental and predicted case

The heat-treated specimen has a better thermal diffusivity than the no treated one.

The explanation is related to the number of voids and pores that are intrinsic in the additive manufacturing process, after the heat treatment at high temperature, the porosities decreases, so the thermal conductivity increases, such as the electric conductivity.

Chapter 7

Conclusion and Future Work

The main objective of this work was to demonstrate the feasibility of producing ferromagnetic components using Additive Manufacturing, particularly the LPBF technique. These components' main implications concern the electrical field applications, therefore electromagnetic or electromechanical devices. From the results obtained and discussed, it can be concluded that:

- It is possible to create dense objects with the FeSi2.9 alloy by optimizing the printing parameters

- The printing parameters and the orientation of the piece affect the electrical and magnetic characteristics of the components produced

- An annealing treatment is necessary to reduce residual tensions due to the production process and to increase the magnetic properties

- To date, the components produced are massive and therefore characterized by high losses due to eddy currents as the operating frequency increases. For this reason, further studies will be required to optimize the topology of the pieces or to vary the printing parameters during the manufacturing process to create parts with different densities.

- Among the limits of technology, in addition to the high cost, we encounter dimensional limits and low production volumes

The work carried out in this thesis lays the foundations for future research on the construction of a reluctance motor for electric traction. The goal will be to make

both the active and passive parts and the windings using the LPBF technique. The study will also concern the various parts' recycling methodologies to conclude the green production system's production cycle.

Bibliography

[1] Jeff Allen. "An Investigation into the Comparative Costs of Additive Manufacture vs. Machine from Solid for Aero Engine Parts". In: *undefined* (2006).

[2] Eleonora Atzeni. "(PDF) Additive manufacturing as a cost-effective way to produce metal parts". In: (). DOI: 10.1201/b15961-3.

[3] P. A. Kobryn et al. *Additive Manufacturing of Aerospace Alloys for Aircraft Structures.* Section: Technical Reports. AIR FORCE RESEARCH LAB WRIGHT-PATTERSON AFB OH MATERIALS AND MANUFACTURING DIRECTORATE, May 1, 2006.

[4] Christiane Beyer. "Strategic Implications of Current Trends in Additive Manufacturing". In: *Journal of Manufacturing Science and Engineering* 136.6 (Dec. 1, 2014). Publisher: American Society of Mechanical Engineers Digital Collection. ISSN: 1087-1357. DOI: 10.1115/1.4028599.

[5] J. K. Watson and K. M. B. Taminger. "A decision-support model for selecting additive manufacturing versus subtractive manufacturing based on energy consumption". In: *Journal of Cleaner Production* 176 (Dec. 17, 2015), pp. 1316–1322. ISSN: 0959-6526. DOI: 10.1016/j.jclepro.2015.12.009.

[6] Douglas Thomas and Stanley W. Gilbert. "Costs and Cost Effectiveness of Additive Manufacturing". In: *NIST* (Dec. 4, 2014). Last Modified: 2021-06-24T00:06-04:00 Publisher: Douglas Thomas, Stanley W. Gilbert.

[7] M. Baumers et al. "A Comparative Study of Metallic Additive Manufacturing Power Consumption". In: Accepted: 2021-09-30T14:33:05Z. University of Texas at Austin, Sept. 23, 2010. DOI: 10.26153/tsw/15198.

[8] Runze Huang et al. "Energy and emissions saving potential of additive manufacturing: the case of lightweight aircraft components". In: *Journal of Cleaner Production* 135 (Nov. 1, 2016), pp. 1559–1570. ISSN: 0959-6526. DOI: 10.1016/j.jclepro.2015.04.109.

[9] Xiang Zhang et al. "An additively manufactured metallic manifold-microchannel heat exchanger for high temperature applications". In: *Applied Thermal Engineering* 143 (Oct. 1, 2018), pp. 899–908. ISSN: 1359-4311. DOI: 10.1016/j.applthermaleng.2018.08.032.

[10] F. Romei, A. N. Grubišić, and D. Gibbon. "Manufacturing of a high-temperature resistojet heat exchanger by selective laser melting". In: *Acta Astronautica* 138 (Sept. 2017), pp. 356–368. ISSN: 0094-5765. DOI: 10.1016/j.actaastro.2017.05.020.

[11] Kathryn L. Kirsch and Karen A. Thole. "Isolating the effects of surface roughness versus wall shape in numerically optimized, additively manufactured micro cooling channels". In: *Experimental Thermal and Fluid Science* 98 (Nov. 1, 2018), pp. 227–238. ISSN: 0894-1777. DOI: 10.1016/j.expthermflusci.2018.05.030.

[12] A. Mazurchevici, D. Nedelcu, and R. Popa. *Additive manufacturing of composite materials by FDM technology: A review*. 2020.

[13] Hans Tiismus et al. "Additive Manufacturing and Performance of E-Type Transformer Core". In: *Energies* 14.11 (Jan. 2021). Number: 11 Publisher: Multidisciplinary Digital Publishing Institute, p. 3278. ISSN: 1996-1073. DOI: 10.3390/en14113278. URL: https://www.mdpi.com/1996-1073/14/11/3278 (visited on 11/05/2022).

[14] Muhammad Usman Naseer et al. "A Review on Additive Manufacturing Possibilities for Electrical Machines". In: *Energies* 14.7 (Jan. 2021). Number: 7 Publisher: Multidisciplinary Digital Publishing Institute, p. 1940. ISSN: 1996-1073. DOI: 10.3390/en14071940. URL: https://www.mdpi.com/1996-1073/14/7/1940 (visited on 11/05/2022).

[15] Rafal Wrobel and Barrie Mecrow. "Additive Manufacturing in Construction of Electrical Machines – A Review". In: *2019 IEEE Workshop on Electrical Machines Design, Control and Diagnosis (WEMDCD)*. Vol. 1. 2019, pp. 15–22. DOI: 10.1109/WEMDCD.2019.8887765.

[16] Andreas Kirchheim, Hans-Jörg Dennig, and Livia Zumofen. "Why Education and Training in the Field of Additive Manufacturing is a Necessity". In: *Industrializing Additive Manufacturing - Proceedings of Additive Manufacturing in Products and Applications - AMPA2017*. International Conference on Additive Manufacturing in Products and Applications. Springer, Cham, 2018, pp. 329–336. DOI: `10.1007/978-3-319-66866-6_31`.

[17] Johnnie Liew Zhong Li et al. "Review of Wire Arc Additive Manufacturing for 3D Metal Printing". In: *International Journal of Automation Technology* 13.3 (May 5, 2019). Publisher: Fuji Technology Press Ltd., pp. 346–353. DOI: `10.20965/ijat.2019.p0346`.

[18] Joe Hiemenz. "Electron beam melting". In: *Advanced Materials & Processes* 165 (2007), pp. 45–46.

[19] L. Loeber et al. "Comparison off Selective Laser and Electron Beam Melted Titanium Aluminides". In: Accepted: 2021-10-05T14:24:15Z. University of Texas at Austin, 2011. DOI: `10.26153/tsw/15316`.

[20] Tuğrul Özel et al. "Focus Variation Measurement and Prediction of Surface Texture Parameters Using Machine Learning in Laser Powder Bed Fusion". In: *Journal of Manufacturing Science and Engineering* 142.1 (Jan. 1, 2020). Publisher: American Society of Mechanical Engineers Digital Collection. ISSN: 1087-1357. DOI: `10.1115/1.4045415`.

[21] Daniel Oropeza and A. John Hart. "A laboratory-scale binder jet additive manufacturing testbed for process exploration and material development". In: *The International Journal of Advanced Manufacturing Technology* 114.11 (June 1, 2021). Company: Springer Distributor: Springer Institution: Springer Label: Springer Number: 11 Publisher: Springer London, pp. 3459–3473. ISSN: 1433-3015. DOI: `10.1007/s00170-021-07123-1`.

[22] Snehashis Pal and Igor Drstvenek. "Physical Behaviors of Materials in Selective Laser Melting Process". In: 2018.

[23] Markus Hofele et al. "Laser Polishing of Laser Powder Bed Fusion AlSi10Mg Parts—Influence of Initial Surface Roughness on Achievable Surface Quality". In: *Materials Sciences and Applications* 12 (Jan. 1, 2021), pp. 15–41. DOI: `10.4236/msa.2021.121002`.

[24] Di Wang et al. "Mechanisms and characteristics of spatter generation in SLM processing and its effect on the properties". In: *Materials & Design* 117 (Mar. 5, 2017), pp. 121–130. ISSN: 0264-1275. DOI: 10.1016/j.matdes. 2016.12.060.

[25] "A short review on selective laser melting of H13 steel". English. In: *The International Journal of Advanced Manufacturing Technology* 108.7-8 (June 2020). Copyright - © Springer-Verlag London Ltd., part of Springer Nature 2020, pp. 2453–2466. URL: https://www.proquest.com/scholarly-journals/short-review-on-selective-laser-melting-h13-steel/docview/2415176535/se-2.

[26] "A Study on the Laser Spatter and the Oxidation Reactions During Selective Laser Melting of 316L Stainless Steel, Al-Si10-Mg, and Ti-6Al-4V: Physical Metallurgical and Materials Science". English. In: *Metallurgical and Materials Transactions* 46.9 (Sept. 2015). Copyright - The Minerals, Metals Materials Society and ASM International 2015; CODEN - MMTAEB, pp. 3842–3851. URL: https://www.proquest.com/scholarly-journals/study-on-laser-spatter-oxidation-reactions-during/docview/1700917937/se-2.

[27] Laura Cordova, Mónica Campos, and Tiedo Tinga. "Revealing the Effects of Powder Reuse for Selective Laser Melting by Powder Characterization". In: *JOM* 71 (2019), pp. 1062–1072.

[28] A. Gatto, E. Bassoli, and L. Denti. "Repercussions of powder contamination on the fatigue life of additive manufactured maraging steel". In: *Additive Manufacturing* 24 (2018), pp. 13–19. ISSN: 2214-8604. DOI: https://doi.org/10.1016/j.addma.2018.09.004. URL: https://www.sciencedirect.com/science/article/pii/S2214860418303270.

[29] Shuai Liu and Hanjie Guo. "Balling Behavior of Selective Laser Melting (SLM) Magnesium Alloy". In: *Materials* 13.16 (Aug. 17, 2020), p. 3632. ISSN: 1996-1944. DOI: 10.3390/ma13163632.

[30] J.P. Oliveira, A.D. LaLonde, and J. Ma. "Processing parameters in laser powder bed fusion metal additive manufacturing". In: *Materials Design* 193 (2020), p. 108762. ISSN: 0264-1275. DOI: https://doi.org/10.1016/j.

matdes.2020.108762. URL: https://www.sciencedirect.com/science/article/pii/S0264127520302963.

[31] Peter Mercelis and J. P. Kruth. "Residual stresses in selective laser sintering and selective laser melting". In: *Rapid Prototyping Journal* 12 (2006), pp. 254–265.

[32] R. Acevedo et al. "Residual stress analysis of additive manufacturing of metallic parts using ultrasonic waves: State of the art review". In: *Journal of Materials Research and Technology* 9.4 (2020), pp. 9457–9477. ISSN: 2238-7854. DOI: https://doi.org/10.1016/j.jmrt.2020.05.092. URL: https://www.sciencedirect.com/science/article/pii/S2238785420313600.

[33] C. Li et al. "Residual Stress in Metal Additive Manufacturing". In: *Procedia CIRP* 71 (2018). 4th CIRP Conference on Surface Integrity (CSI 2018), pp. 348–353. ISSN: 2212-8271. DOI: https://doi.org/10.1016/j.procir.2018.05.039. URL: https://www.sciencedirect.com/science/article/pii/S221282711830667X.

[34] J.P. Kruth et al. "Selective laser melting of iron-based powder". Undefined. In: *Journal of materials processing technology* 149.1-3 (2004), pp. 616–622. ISSN: 0924-0136.

[35] Haolin Jia et al. "Scanning strategy in selective laser melting (SLM): a review". In: *The International Journal of Advanced Manufacturing Technology* 113 (Apr. 1, 2021). DOI: 10.1007/s00170-021-06810-3.

[36] Lindsay M. Sochalski-Kolbus et al. "Comparison of Residual Stresses in Inconel 718 Simple Parts Made by Electron Beam Melting and Direct Laser Metal Sintering". In: *Metallurgical and Materials Transactions A* 46 (2015), pp. 1419–1432.

[37] Mitun Das et al. "Laser processing of SiC-particle-reinforced coating on titanium". eng. In: *Scripta materialia* 63.4 (2010), pp. 438–441. ISSN: 1359-6462.

[38] William H. Hofmeister and Michelle L. Griffith. "Solidification in direct metal deposition by LENS processing". In: *JOM* 53 (2001), pp. 30–34.

[39] Dongdong Gu and Yifu Shen. "Balling phenomena in direct laser sintering of stainless steel powder: Metallurgical mechanisms and control methods". In: *Materials & Design* 30 (2009), pp. 2903–2910.

[40] Jean-Pierre Kruth et al. *Selective laser melting of iron-based powder*. eng. 2004-06-01.

[41] A Simchi and H Pohl. "Effects of laser sintering processing parameters on the microstructure and densification of iron powder". In: *Materials Science and Engineering: A* 359.1 (2003), pp. 119–128. ISSN: 0921-5093. DOI: https://doi.org/10.1016/S0921-5093(03)00341-1. URL: https://www.sciencedirect.com/science/article/pii/S0921509303003411.

[42] Dongdong Gu et al. "Selective Laser Melting of in-situ TiC/Ti5Si3 composites with novel reinforcement architecture and elevated performance". In: *Surface & Coatings Technology* 205 (2011), pp. 3285–3292.

[43] Prince Cobbinah et al. "Laser Powder Bed Fusion of Potential Superalloys: A Review". In: *Metals* 11 (Dec. 30, 2020), p. 58. DOI: 10.3390/met11010058.

[44] E.O. Olakanmi, R.F. Cochrane, and K.W. Dalgarno. "A review on selective laser sintering/melting (SLS/SLM) of aluminium alloy powders: Processing, microstructure, and properties". In: *Progress in Materials Science* 74 (2015), pp. 401–477. ISSN: 0079-6425. DOI: https://doi.org/10.1016/j.pmatsci.2015.03.002. URL: https://www.sciencedirect.com/science/article/pii/S0079642515000389.

[45] "Densification mechanism and microstructural evolution in selective laser sintering of Al12Si powder has been explored. It was established that both the densification mechanism and microstructural evolution in laser sintered Al12Si powders indicated that the tops of the grains in the previous layer are partially re-melted and then undergo epitaxial growth in the next layer where the heat affected zones (HAZ) grain boundaries and solidification grain boundaries (SGBs) are continuous along the fusion boundary." In: ().

[46] P. Krakhmalev and I. Yadroitsev. "Microstructure and properties of intermetallic composite coatings fabricated by selective laser melting of Ti–SiC powder mixtures". In: *Intermetallics* 46 (2014), pp. 147–155. ISSN: 0966-9795. DOI: https://doi.org/10.1016/j.intermet.2013.11.012. URL: https://www.sciencedirect.com/science/article/pii/S0966979513003117.

[47] Weihao Yuan et al. "Effects of laser scanning speeds on different states of the molten pool during selective laser melting: Simulation and experiment". In: *Materials Design* 189 (2020), p. 108542. ISSN: 0264-1275. DOI: https://doi.

org/10.1016/j.matdes.2020.108542. URL: https://www.sciencedirect.com/science/article/pii/S0264127520300757.

[48] Ruidi Li et al. "Balling behavior of stainless steel and nickel powder during selective laser melting process". In: *The International Journal of Advanced Manufacturing Technology* 59.9-12 (2012), pp. 1025–1035. DOI: 10.1007/s00170-011-3566-1. URL: https://app.dimensions.ai/details/publication/pub.1023499442.

[49] Abdolreza Simchi and Hamed Asgharzadeh. "Densification and microstructural evaluation during laser sintering of M2 high speed steel powder". In: *Materials Science and Technology* 20 (2004), pp. 1462–1468.

[50] I. Yadroitsev et al. "Single track formation in selective laser melting of metal powders". In: *Journal of Materials Processing Technology* 210.12 (2010), pp. 1624–1631. ISSN: 0924-0136. DOI: https://doi.org/10.1016/j.jmatprotec.2010.05.010. URL: https://www.sciencedirect.com/science/article/pii/S0924013610001469.

[51] Lore Thijs et al. "A study of the microstructural evolution during selective laser melting of Ti4V". In: *Acta Materialia* 58.9 (2010), pp. 3303–3312. ISSN: 1359-6454. DOI: https://doi.org/10.1016/j.actamat.2010.02.004. URL: https://www.sciencedirect.com/science/article/pii/S135964541000090X.

[52] W-N Su, P Erasenthiran, and P M Dickens. "Investigation of fully dense laser sintering of tool steel powder using a pulsed Nd: Yag (neodymium-doped yttrium aluminium garnet) laser". In: *Proceedings of the Institution of Mechanical Engineers, Part C: Journal of Mechanical Engineering Science* 217.1 (2003), pp. 127–138. DOI: 10.1243/095440603762554677. eprint: https://doi.org/10.1243/095440603762554677. URL: https://doi.org/10.1243/095440603762554677.

[53] Prince Valentine Cobbinah et al. "Laser Powder Bed Fusion of Potential Superalloys: A Review". In: *Metals* 11.1 (2021). ISSN: 2075-4701. DOI: 10.3390/met11010058. URL: https://www.mdpi.com/2075-4701/11/1/58.

[54] Mohsen Badrossamay et al. *Improving Productivity Rate in SLM of Commercial Steel Powders.* eng. 2009-05-01.

[55] A.B. Spierings, N. Herres, and G. Levy. "Influence of the particle size distribution on surface quality and mechanical properties in AM steel parts". In: *Rapid Prototyping Journal* 17.3 (Jan. 1, 2011). Ed. by Dave Bourell and Brent Stucker. Publisher: Emerald Group Publishing Limited, pp. 195–202. ISSN: 1355-2546. DOI: 10.1108/13552541111124770. URL: https://doi.org/10.1108/13552541111124770 (visited on 09/19/2022).

[56] Luke N. Carter et al. "The influence of the laser scan strategy on grain structure and cracking behaviour in SLM powder-bed fabricated nickel superalloy". In: *Journal of Alloys and Compounds* 615 (2014), pp. 338–347. ISSN: 0925-8388. DOI: https://doi.org/10.1016/j.jallcom.2014.06.172. URL: https://www.sciencedirect.com/science/article/pii/S092583881401528X.

[57] D. Goll et al. "Additive manufacturing of soft magnetic materials and components". In: *Additive Manufacturing* 27 (May 1, 2019), pp. 428–439. ISSN: 2214-8604. DOI: 10.1016/j.addma.2019.02.021.

[58] Tomas F. Babuska et al. "Achieving high strength and ductility in traditionally brittle soft magnetic intermetallics via additive manufacturing". In: *Acta Materialia* 180 (2019), pp. 149–157. ISSN: 1359-6454. DOI: https://doi.org/10.1016/j.actamat.2019.08.044. URL: https://www.sciencedirect.com/science/article/pii/S1359645419305646.

[59] T. N. Lamichhane et al. "Additive manufacturing of soft magnets for electrical machines—a review". In: *Materials Today Physics* 15 (Dec. 1, 2020), p. 100255. ISSN: 2542-5293. DOI: 10.1016/j.mtphys.2020.100255.

[60] Michele Garibaldi. "Metallurgy of high-silicon steel parts produced using Selective Laser Melting". In: *Acta Materialia* 110 (May 15, 2016). Publisher: Pergamon, pp. 207–216. ISSN: 1359-6454. DOI: 10.1016/j.actamat.2016.03.037.

[61] Michele Garibaldi. "Relationship between laser energy input, microstructures and magnetic properties of selective laser melted Fe-6.9%wt Si soft magnets". In: *Materials Characterization* 143 (Sept. 1, 2018). Publisher: Elsevier, pp. 144–151. ISSN: 1044-5803. DOI: 10.1016/j.matchar.2018.01.016.

[62] H. Shokrollahi and K. Janghorban. "Soft magnetic composite materials (SMCs)". In: *Journal of Materials Processing Technology* 189.1 (2007), pp. 1–12. ISSN: 0924-0136. DOI: https://doi.org/10.1016/j.jmatprotec.2007.02.034. URL: https://www.sciencedirect.com/science/article/pii/S0924013607001756.

[63] J. N. Lemke et al. "Calorimetric study and microstructure analysis of the order-disorder phase transformation in silicon steel built by SLM". In: *Journal of Alloys and Compounds* 722 (Oct. 25, 2017), pp. 293–301. ISSN: 0925-8388. DOI: 10.1016/j.jallcom.2017.06.085.

[64] Y. Takada et al. "Commercial scale production of Fe-6.5 wt. % Si sheet and its magnetic properties". In: *Journal of Applied Physics* 64.10 (Nov. 1988), pp. 5367–5369. DOI: 10.1063/1.342373.

[65] H. Haiji et al. "Magnetic properties and workability of 6.5% Si steel sheet". In: *Journal of Magnetism and Magnetic Materials* 160 (1996). Proceedings of the twelfth International Conference on Soft Magnetic Materials, pp. 109–114. ISSN: 0304-8853. DOI: https://doi.org/10.1016/0304-8853(96)00128-X. URL: https://www.sciencedirect.com/science/article/pii/030488539600128X.

[66] Gaoyuan Ouyang et al. "Review of Fe-6.5wt%Si high silicon steel—A promising soft magnetic material for sub-kHz application". In: *Journal of Magnetism and Magnetic Materials* 481 (July 1, 2019), pp. 234–250. ISSN: 0304-8853. DOI: 10.1016/j.jmmm.2019.02.089.

[67] Tanya Ros-Yanez et al. "Study of deformation and aging behaviour of iron–silicon alloys". In: *Materials Science and Engineering: A* 447.1 (2007), pp. 27–34. ISSN: 0921-5093. DOI: https://doi.org/10.1016/j.msea.2006.10.075. URL: https://www.sciencedirect.com/science/article/pii/S0921509306022520.

[68] B. Viala et al. "Study of the brittle behaviour of annealed Fe-6.5 wt%Si ribbons produced by planar flow casting". In: *Materials Science and Engineering: A* 212.1 (1996), pp. 62–68. ISSN: 0921-5093. DOI: https://doi.org/10.1016/0921-5093(96)10188-X. URL: https://www.sciencedirect.com/science/article/pii/092150939610188X.

[69] Pyungwoo Jang, Bonghan Lee, and Gwangbo Choi. "Effects of annealing on the magnetic properties of Fe-6.5%Si alloy powder cores". In: *Journal of Applied Physics* 103 (2008).

[70] Fernando González and Yvan Houbaert. "A review of ordering phenomena in iron-silicon alloys". In: 2013.

[71] Erik J. Hilinski and Gwynne H. Johnston. "Annealing of electrical steel". In: *2014 4th International Electric Drives Production Conference (EDPC)* (2014), pp. 1–7.

[72] M. Garibaldi et al. "Effect of annealing on the microstructure and magnetic properties of soft magnetic Fe-Si produced via laser additive manufacturing". In: *Scripta Materialia* 142 (2018), pp. 121–125. ISSN: 1359-6462. DOI: https://doi.org/10.1016/j.scriptamat.2017.08.042. URL: https://www.sciencedirect.com/science/article/pii/S1359646217305067.

[73] Luca Ferraris et al. "Effect of the Temperature on the Magnetic and Energetic Properties of Soft Magnetic Composite Materials". In: *Energies* 14.15 (Jan. 2021). Number: 15 Publisher: Multidisciplinary Digital Publishing Institute, p. 4400. ISSN: 1996-1073. DOI: 10.3390/en14154400.

[74] Marco Grasso and Bianca Maria Colosimo. "Process defects and in situ monitoring methods in metal powder bed fusion: a review". In: *Measurement Science and Technology* 28 (2017).

[75] Ian D. Harris. "Development and implementation of metals additive manufacturing". In: 2017.

[76] "Measurement Science Roadmap for Metal-Based Additive Manufacturing". In: (), p. 86.

[77] *nondestructive evaluation of additive manufacturing state-of-the-discipline report - NASA Technical Reports Server (NTRS).* URL: https://ntrs.nasa.gov/citations/20140016447 (visited on 09/19/2022).

[78] Hossein Taheri et al. "Powder-based additive manufacturing – a review of types of defects, generation mechanisms, detection, property evaluation and metrology". In: 2017.

[79] Daniel Chauveau. "Review of NDT and process monitoring techniques usable to produce high-quality parts by welding or additive manufacturing". In: *Welding in the World* 62 (2018), pp. 1097–1118.

[80]   Ana Lopez et al. "Mapping of non-destructive techniques for inspection of wire and arc additive manufacturing". In: June 11, 2017.

[81]   Angela Cantatore and Pavel Müller. *Introduction to computed tomography.* English. DTU Mechanical Engineering, 2011.

This Ph.D. thesis has been typeset by means of the T_EX-system facilities. The typesetting engine was pdfL^AT_EX. The document class was `toptesi`, by Claudio Beccari, with option `tipotesi=scudo`. This class is available in every up-to-date and complete T_EX-system installation.